Martini 3 Coarse-Grained Force Field for cholesterol

Luís Borges-Araújo[1,2]; Ana C. Borges-Araújo[1]; Tugba Nur Ozturk[3]; Daniel P. Ramirez-Echemendia[4], Balázs Fábián[5], Timothy S. Carpenter[3]; Sebastian Thallmair[6], Jonathan Barnoud[7,8]; Helgi I. Ingólfsson[3]; Gerhard Hummer[5,9]; D. Peter Tieleman[4]; Siewert J. Marrink[10]; Paulo C. T. Souza[2,*]; Manuel N. Melo[1,*]

1. Instituto de Tecnologia Química e Biológica António Xavier, Universidade Nova de Lisboa, Av. da República, 2780-157, Oeiras, Portugal;
2. Molecular Microbiology and Structural Biochemistry, UMR 5086 CNRS & University of Lyon, 7 Passage du Vercors, Lyon F-69367, France;
3. Physical and Life Sciences (PLS) Directorate, Lawrence Livermore National Laboratory, Livermore, CA, 94550, USA;
4. Centre for Molecular Simulation and Department of Biological Sciences, University of Calgary, Alberta, Canada;
5. Department of Theoretical Biophysics, Max Planck Institute of Biophysics, Max-von-Laue Straße 3, 60438 Frankfurt am Main, Germany;
6. Frankfurt Institute for Advanced Studies, Ruth-Moufang-Straße 1, 60438 Frankfurt am Main, Germany;
7. Centre for Computational Chemistry, School of Chemistry, University of Bristol, Cantock's Close, Bristol BS8 1TS, UK;
8. CiTIUS Intelligent Technologies Research Centre, University of Santiago de Compostela, Rúa de Jenaro de la Fuente, 15705 Santiago de Compostela, Spain;
9. Institute of Biophysics, Goethe University Frankfurt, 60438 Frankfurt am Main, Germany;
10. Groningen Biomolecular Sciences and Biotechnology Institute, University of Groningen, Nijenborgh 7, 9747 AG Groningen, The Netherlands.

* Corresponding authors: Manuel N. Melo - m.n.melo@itqb.unl.pt
Paulo C.T. Souza - paulocts@gmail.com

Abstract

Cholesterol plays a crucial role in biomembranes by regulating various properties such as fluidity, rigidity, permeability, and organization of lipid bilayers. The latest version of the Martini model, Martini 3, offers significant improvements in interaction balance, molecular packing, and the inclusion of new bead types and sizes. However, the release of the new model resulted in the need to re-parameterize many core molecules, including cholesterol. Here, we describe the development and validation of a Martini 3 cholesterol model, addressing issues related to its bonded setup, shape, volume and hydrophobicity. The proposed model mitigates some limitations of its Martini 2 predecessor while maintaining or improving overall behavior.

Keywords: Martini 3; Cholesterol; Membrane simulations; Molecular dynamics

1. Introduction

Cholesterol is an important and crucial biomolecule, predominantly localized at animal cell membranes where it serves as an essential regulator of lipid bilayer fluidity, rigidity, and permeability[1,2]. Cholesterol also plays an important role in modulating lipid lateral organization by promoting the formation of liquid-ordered phases[2,3]. As such, it has been implicated as one of the main components in the lipid raft hypothesis[4]. The impact of cholesterol extends beyond the lipid membrane, as it can interact with a variety of proteins, acting as a necessary cofactor for the correct functioning of several processes[5,6]. Metabolically, cholesterol is also a direct precursor of steroid hormones[2], such as progesterone, testosterone, cortisol, and estrogens. While cholesterol is predominant in animal cells, other related sterol compounds play similar relevant roles in other

kingdoms[2], such as phytosterols in plants, ergosterol in fungi, and hopanoids in bacteria. Additionally, cholesterol and other cholesterol-based molecules have recently piqued biotechnological interest, as they have been shown to be crucial components in the liposome-nucleic acid complexes deployed as delivery systems in gene therapy and mRNA-based vaccines[7,8].

Molecular dynamics (MD) simulations provide molecular-level structural detail into the dynamics of cellular processes and systems which may not be fully accessible with experimental techniques. MD has allowed researchers to probe specific interactions between cholesterol and other membrane partners such as lipids or proteins; particular biophysical properties such as flip-flop, interdigitation or membrane permeability; study phase-separation and the formation of lipid domains; cholesterol-mediated protein sorting; and even the biophysical properties of curved lipid membranes. Overall, MD studies have offered a more detailed view and better understanding of cholesterol biophysics[9–15]. Coarse-grained (CG) MD simulation methods, such as Martini[16,17], can take these studies one step further, allowing for simulations of systems at micrometer and millisecond scales while maintaining near-atomic level detail.

The Martini model[16,17] is one of the most widely used CG force fields for biomolecular simulations, particularly in the modeling of biomembrane systems. In a large part of these successful biomembrane studies, cholesterol played a key role. Martini has been successfully applied in the study of phase behavior in model membranes, where complete lipid phase diagrams have been established for binary lipid/cholesterol systems, as well as ternary and even quaternary lipid mixtures[18–24]. The force field has also seen extensive use in identifying lipid binding sites on the surface of membrane proteins, where the study of cholesterol binding sites on GPCRs has been one of the hottest topics[12,25]. Studies on the interactions between proteins and lipids have not been limited to identifying binding sites, but have also focused on other lipid-mediated effects that can modulate protein-protein interactions[26–30]. The size and time scales within reach of Martini have also allowed for the study of processes otherwise inaccessible. These range from membrane, vesicle and/or nanoparticle fusion studies[31–34], to large-scale membrane curvature studies[35–39]. The realistic large-scale Martini simulations of both an average mammalian plasma membrane[40], and a neuronal plasma membrane[41] stand out as some of the most complex biomolecular simulations to date[42] . The average mammalian plasma membrane was composed of 63 different lipid types (including cholesterol), with 15 different headgroups and 11 different tails.

As Martini 2[17] became a standard tool, some less obvious faults in the force field became apparent[43], specifically in cases where the underlying AA-to-CG mappings were finer than 4 heavy atoms to 1 CG bead or when intermolecular bead-bead distances were very short. These led to a number of issues, the most important being that some molecules, in particular proteins[44,45] and ring structures (such as carbohydrates[46]), displayed excessive hydrophobicity and self-interaction[43]. These pitfalls prompted a new and improved version of Martini – Martini 3, released in 2021[16] – to address some of these shortcomings. Martini 3 introduced new bead sizes specific for mappings finer than 4-to-1 and defined a larger number of bead types, greatly increasing the discrimination of chemical space. Alongside the new bead types and sizes, the model also introduced new guidelines for the parameterization of new molecules which resulted in the need to update and improve many of the previously modeled biomolecules. At the moment, only proteins[16], common phospholipids[16], phosphoinositides[47], some glycolipids[48], carbohydrates[48,49], small molecules[50] and green solvents[51,52] have been included in the Martini 3 database[53]. The general Martini 2 shortcomings also affected cholesterol, which was excessively lipophilic[54]. In addition, an issue specific to the Martini 2 cholesterol model was encountered in which temperature artifacts were observed due to convergence issues with the linear constraints solver (LINCS) algorithm[55]. These aspects were found

to have a substantial impact on cholesterol properties in membranes and their interactions with other partners[54–56].

Overall, the Martini 2 cholesterol model has shown great success in the many applications it has been used in. However, it is now clear that there is a need for a finer reparameterization effort, that not only brings it up to date with the Martini 3 framework but also addresses many of the reported cholesterol-specific issues. In this work, we successfully develop and validate a Martini 3 CG model of cholesterol. Cholesterol shape and volume, hydrophobicity, and temperature divergence issues due to the bonded setup were addressed in detail. We arrive at a model that mitigates some limitations of its predecessor while maintaining or improving overall behavior as much as possible.

2. Methods

All simulations were run using the GROMACS[57] simulation package version 2020 and analyzed with in-house developed Python 3 programs using the MDAnalysis package[58,59]. We also used the IPython[60], numpy[61], SciPy[62], scikit-learn[63], Voro++[64], and matplotlib[65] packages for scientific computing in Python. Visualization and rendering of the simulations were performed with the molecular graphics viewer VMD[66]. Analysis methods part of the GROMACS tool suite were also used[57]. Octanol−water partition free energies were calculated from the individual CG solvation free energies into each solvent, as described elsewhere[67]. See the Methods section of the Supporting Information for details on specific analysis methods.

2.1. Atomistic Models. All atomistic models used as the parameterization targets were simulated using the CHARMM36 force field[68,69], with the TIP3P water model. All topologies used are readily available in CHARMM-GUI[70,71]. To validate the parameterization of cholesterol, simulations were performed of cholesterol either in water or inserted in a lipid bilayer.

For cholesterol simulations in water, a single cholesterol molecule was inserted in a 3 × 3 × 3 nm^3 simulation box, which was then fully solvated. For the lipid membrane systems, initial structures were generated using the CHARMM-GUI membrane builder module[72–74] by arranging the lipids on a regular array in the bilayer (xy) plane. Membranes were built with roughly 260 lipids per leaflet, which were then solvated by ~22,000 water molecules. Lipid membrane compositions tested are summarized in the supplementary material (Table S1). Every system was neutralized and an additional 140 mM NaCl was added.

After initial energy minimization and equilibration runs, all atomistic simulations were run at a 2 fs time step. The LINCS[75] algorithm was applied to constrain all, non-water, bonded hydrogens. Van der Waals forces were switched off smoothly from 1.0 to 1.2 nm, and electrostatics were computed using particle-mesh Ewald summation[76]. The particle neighbor list was updated using the Verlet list scheme. The system temperature was maintained at 310 K by coupling to a Nosé−Hoover thermostat[77] with a 1 ps coupling constant, while pressure was coupled to 1.0 bar using a Parrinello−Rahman barostat[78] (isotropically for aqueous systems, semi-isotropically for membrane systems) with a 5 ps coupling time. All atomistic simulations were run for at least 1 μs.

2.2. Coarse-Grained Models. All coarse-grained simulations were modeled using either the Martin 2[17] or Martini 3 CG models[16]. All topologies, other than the cholesterol topology parameterized here, were released alongside the force field[16]. Along this text, bead names will be typed in italics, to distinguish them from bead types.

To validate the cholesterol model, CG simulations were performed of either a single cholesterol molecule in water or several inserted in lipid bilayer systems. For cholesterol simulations in water, a single cholesterol molecule was inserted in a 3 × 3 × 3 nm^3 simulation box, which was then fully solvated. For the lipid membrane systems, initial structures were built and solvated using the insane.py CG building tool[79] by arranging the lipids and cholesterol on a regular array in the bilayer (xy) plane to obtain approximately 2000 lipids per leaflet, solvated by roughly 27,000 water beads. Hexagonal periodic boundary conditions were used when necessary to avoid packing defects upon gel-phase formation. Lipid membrane compositions tested are summarized in the supplementary material (Table S1). All CG systems were solvated with regular Martini water beads. Counterions were added to neutralize the systems as necessary, plus 140 mM NaCl ionic strength. Additionally, CG simulations of two cholesterol crystal structures were performed. The atomistic crystal structures of cholesterol (CCDC code: CHOEST20[80]) and cholesterol monohydrate (CCDC code: CHOLES20[81]) were coarse-grained and used to construct supercells of size 3 × 2 × 4 and 3 × 3 × 2 nm^3, respectively.

Three different proteins were also studied. Protein structures were obtained from the Protein Data Bank[82] (PDB). The G Protein-Coupled Receptor Smoothened (SMO) model used in our simulations was based on the near full-length structure (PDB: 5L7D[83]) and prepared as described elsewhere[84]. The voltage-dependent anion channel 2 (VDAC2) model used in our simulations was based on a well-resolved structure of mouse VDAC1 (PDB: 4C69[85]) and prepared as described elsewhere[86]. The β_2-adrenergic receptor (β_2AR) model used in our simulations was based on the full-length structure (PDB: 3D4S[87]) and prepared similarly to SMO. All CG protein models were constructed using Martinize2[88], with an applied elastic network with a bond force constant of 700 kJ/mol and a cutoff distance of 0.8 nm. Side chain corrections were also applied[89]. Both SMO and VDAC2 models were positioned in the membrane roughly as described in previous simulation studies[84,86]. All proteins were simulated in POPC:CHOL membranes at 85:15 mol% ratios.

Nonbonded interactions were cut off at 1.1 nm, and Coulombic interactions were treated using reaction-field electrostatics[90] with a dielectric constant of 15 and an infinite reaction-field dielectric constant. The particle neighbor list was updated using the Verlet list scheme. A v-rescale thermostat[91] was used with a coupling time of 4.0 ps to maintain the temperature at 300 K (unless other temperatures are specified). A constant pressure of 1.0 bar was established by isotropic or semi-isotropic (in the case of membranes) coupling to a Parrinello−Rahman barostat[78] with a relaxation time of 16.0 ps. After initial energy minimization and pressure/temperature equilibration runs, simulations were run at a 20 fs time step. Stability runs were carried out with either a 30 or 40 fs time step. To avoid numerical stability issues, ions were not added in the stability runs[92]. The LINCS[75] algorithm was used to solve bonded constraints using *lincs_order = 4* and *lincs_iter = 1*. For Martini 2 simulations, *lincs_order = 12* and *lincs_iter = 2* were used to avoid artificial temperature gradients due to non converged constraints[55]. All CG systems were run for at least 10 μs, and unless otherwise stated, the last 2 μs of each simulation was used for subsequent analysis. Simulations containing proteins were run for at least 30 μs. For the crystal structure simulations, the supercells were minimized and equilibrated in temperature steps of 50 K beginning at 50 K until the desired temperature for production was reached. Production simulations were performed at 200 K and 295 K with the latter being the temperature of the experimental measurements. The time step of the

production simulations was 1 fs, equilibrations were performed at 0.5 fs (50 K, 100 K) and 1 fs (150 K, 200 K, 250 K), respectively. All simulations were performed without shear stress[93]. For the simulations of cholesterol monohydrate, the water molecules were represented by tiny water beads. The hydrogen bond network was represented by harmonic bonds (750 kJ·mol^{-1}·nm^{-2}) of type 6 in GROMACS which do not exclude non-bonded interactions.

Simulations run with OpenMM[94,95] shared all of the MD setup parameters with their GROMACS counterparts, with the exception of using a different constraint algorithm. Constant Constraint Matrix Approximation (CCMA) was used instead of LINCS. The Martini implementation in OpenMM has been shown to offer excellent agreement between OpenMM and GROMACS in single-step force and energy calculations, with only small differences arising in ensemble averages[95].

The developed cholesterol model is provided as a GROMACS-compatible topology file (including beta versions distributed to the modeling community for testing) and as supporting Information associated with this manuscript. Current and future parameter iterations can be tracked in the associated GitHub repository at https://github.com/Martini-Force-Field-Initiative/M3-Sterol-Parameters, as well as in the MArtini Database web server[53] (MAD - www.mad.ibcp.fr).

3. Results

Our goal with this reparameterization effort was not just to revisit the previous Martini 2.2 cholesterol model[96] and bring it up to date with the new Martini 3 framework[16], but also to address some of its issues, namely, the temperature artifacts observed due to convergence issues with the linear constraints solver (LINCS) algorithm[55,56] and the excessive lipophilicity[54]. The changes made to the model were done in such a way as to maintain or improve the characteristics of the previous model as much as possible, ensuring it retains the biophysical properties that were already correctly recovered.

3.1. Mapping of the cholesterol ring structure and definition of bonded parameters. While the mapping for our Martini 3 cholesterol model is inspired by the Martini 2 version[17,96], some substantial modifications were done to the bead layout. These modifications were made possible due to the most recent iteration of the force field allowing for mappings finer than 4-to-1[16], which was not previously possible, at least not in a systematic manner[43]. Bonded parameter distributions for the model can be found in the Supplementary Figure S1.

3.1.1. Improved cholesterol shape

To better represent the underlying atomistic cholesterol reference structure, two *tiny* beads were added to the layout on the cholesterol rough side (Figure 1 a,b,c). These two beads (*R5* and *R6*) directly account for the two methyl groups that protrude axially relative to the sterol core. The remaining beads of the sterol core (*ROH*, *R1*, *R2*, *R3,* and *R4*) were then placed to match the underlying atomistic solvent accessible surface area (SASA) (Figure 1 a,b,d) and avoid very short intramolecular bead−bead distances, as recommended in the Martini 3 parameterization guidelines[16,50]. *Small* beads were used to construct the cholesterol core (*R1*, *R2*, *R3,* and *R4*) except for the terminal hydroxyl core (*ROH*). The latter as well as the aliphatic chain (*C1*, and *C2*) were described as *regular* beads. The Martini 2 cholesterol topology accounted for the off-ring methyl groups by controlling the protrusion of the corresponding CG beads[96]. However, this approach

cannot fully recover the atomistic cholesterol shape without compromising the planarity of the sterol core and creating pockets on the cholesterol surface opposite the methyl groups (smooth side). As will be seen in the following sections, the new updated bead layout ensures a more accurate packing of cholesterol within the lipid acyl chain structure compared to the Martini 2 model.

3.1.2. Single-frame virtual site topology

In Martini 2, the 8-particle cholesterol layout was connected via a dual-frame virtual site approach[96]. This approach consisted of two triangular frames of constraints (*ROH, R3, R4* & *R3, R4, C1*) sharing an edge (*R3* - *R4*) where they were allowed some freedom to hinge on[96]. The remaining cholesterol core beads (*R2, R1, R5*) were implemented as virtual interaction sites, where their positions were specified as a function of the position of their corresponding constraint frame beads. This topology was intended to improve numerical stability when compared to its predecessor — which was modeled as a stiff mesh of bonds and linear constraints[96]. At the time, a dual-frame topology was chosen over a single-frame alternative due to its shock absorbing properties. The hinge between the two triangular constraint frames effectively worked as a shock absorber that prevented rigid-body displacements from spanning the length of the molecule when simulating at large time steps (40 fs), thus increasing stability at multi-microsecond timescales. Additionally, each of the dual-frame triangles was less acute than the single-frame alternative. This meant the frames' centers of mass became located farther from any one edge, thus avoiding rotation axes with very low moment of inertia (a likely source of the destabilizing high amplitude displacements observed with the single-frame model). However, CG MD lipid bilayer simulations using the highly constrained dual-frame topology have since been shown to cause artificial temperature gradients between molecule types when using standard Martini simulation parameters in GROMACS[55]. Loosely solved constraints in the cholesterol dual-frame topology were identified as the source of this temperature difference, which was seen to impact phase separation, area compressibility, and lipid tail order[55]. This temperature gradient could be suppressed by modifying the LINCS parameters to improve the convergence of the constraint algorithm, but not without impacting performance by 10 to 25 % depending on the system[55].

To address this issue, we reverted our model to a single-frame virtual site approach (Figure 1, c). In this approach beads *R1*, *R2,* and *C1* defined a single rigid triangular frame, assembled using linear constraints. These beads were also used as the constructing particles from which the remaining beads (other than *C2*) were defined as out-of-plane virtual sites. Importantly, this single-frame model is not impacted by LINCS convergence issues (Supplementary Figure S2). Naturally, time integration stability was a concern: the single-frame virtual site approach had also been explored during the Martini 2 cholesterol development process (using the *ROH*, *R3,* and *R4* beads), but was ruled out in favor of the dual-frame approach due to instability at multi-microsecond timescales[96]. In our Martini 3 model, the choice of beads for the rigid triangular frame yielded a more stable topology, with no instabilities being observed for 25 × 25 nm^2 membrane bilayers containing 306 cholesterol molecules simulated over 100 μs using a 40 fs timestep. The increased stability of the single-frame model compared to its Martini 2 counterpart is a welcome consequence of the novel focus of Martini 3 in the reproduction of solvent-excluded volumes: particles are now placed closer to the molecular surface than if they were placed at the center of mass of the represented atoms, as was the case with Martini 2. Because of this, the single frame in our model is a much less acute triangle than the single frame in Martini 2, without rotation axes of problematically small moments of inertia.

While the single-frame virtual site approach loses some flexibility compared to the dual-frame approach it still proved to be a good enough approximation in the coarse grain scale, yielding a good compromise between cholesterol self RMSD, model stability, and temperature convergence

(Supplementary Figure S2). No significant impact on the biophysical properties of cholesterol or cholesterol-containing lipid membranes was observed due to this new arrangement, as seen in the following sections.

Parameters for virtual site construction were obtained from an AA CHARMM36 MD trajectory of cholesterol in a DOPC bilayer. The cholesterol ring particles were CG-mapped as described in the supplementary information (Supplementary Table S4). The positions of the particles were then averaged after rotationally and translationally fitting the entire molecule to the *R1—R2—C1* frame. The placement of the beads relative to bead *C1* was then decomposed as a function of vectors *R1—R2*, *R1—C1*, and of their cross product. Nonbonded interactions between the virtual site particles and between them and the frame particles were switched off. For each bead, Martini bead masses were used, instead of the underlying atomic masses, for better agreement with the Martini 3 lipid models. All bead masses were then redistributed from the virtual site beads to the remaining non virtual site beads. See the supplementary material for more details on the virtual site construction.

3.1.3. Cholesterol aliphatic chain dynamics

The aliphatic chain dynamics of our atomistic cholesterol reference could not be fully captured when using a single angle potential along beads *R5–C1–C2*, as was the case with Martini 2, and instead required a dihedral potential in place. This is likely due to the differences in interaction radii between the different Martini 3 bead sizes that allow for closer interactions and increased configurational freedom compared to Martini 2[16]. The *R6–R4–R3–C2* improper dihedral and *R4–R3–C2* angle potentials were added in place with enough flexibility to account for the dynamics of cholesterol both in a lipid membrane and in solution (Supplementary Figure S1). The potentials were selected so as to minimize the probability of issues from numerical instabilities arising from angles associated with dihedrals reaching 0 or 180 degrees[97].

3.1.4. Implementation in OpenMM

While the new Martini 3 cholesterol model was initially developed and implemented in GROMACS, it has also been successfully ported to OpenMM. During the implementation of the Martini 2 cholesterol model in OpenMM[94], difficulties were encountered with the software's algorithm for handling topology constraints[95]. Unlike GROMACS, which utilizes the LINCS algorithm[75], OpenMM adopts the Constant Constraint Matrix Approximation (CCMA) for constraint treatment[98]. This approach involves the construction of a matrix that characterizes the coupling between constraints based on bonds and angles in the topology. For any pair of constraints that share an atom, a triangle defining an angle, bond, or third constraint is essential in determining the coupling between them according to the CCMA algorithm. Consequently, the topology of the Martini 2 cholesterol model, which features two triangular frames of constraints sharing an edge, causes instability with the CCMA algorithm. Along with the improvements already described, the bonded topology used in the new Martini 3 cholesterol model also ensures compatibility with the CCMA constraint algorithm within the OpenMM platform. By using a single-frame virtual site approach for the topology, which relies on a single triangle of constraints, the coupling between elements in the constraint matrix in the CCMA algorithm can be properly defined, thereby ensuring its stability. The accuracy of the implementation of the new cholesterol model in OpenMM was evaluated using two approaches: *i- single-point calculations*; and *ii- determination of membrane biophysical properties in equilibrium in lipid mixtures with increasing cholesterol concentrations*.

A test case with a single copy of the new Martini 3 cholesterol model in vacuum was added to the battery of single-point tests defined in the *martini_openmm* library 2 (https://github.com/maccallumlab/martini_openmm). This test system for single-point calculations compares energies and forces extracted from simulations carried out with GROMACS version 2021.2 compiled in double precision[57] and OpenMM version 7.5 in double precision mode with the "Reference" platform[94]. The results for the total potential energy were considered to be in agreement, as the absolute error was less than 10^{-3} kJ/mol and the relative error less than 10^{-5}. As for the forces, they were also considered in agreement since all absolute errors after setting OpenMM forces on virtual sites to zero are within 10^{-4} kJ/mol/nm, and all relative errors are less than 10^{-5}. The cutoff values used in this study were selected to fall within the range of differences observed between the implementations of the same CHARMM force field in different simulation engines such as CHARMM, NAMD, and GROMACS[99,100], as discussed in the *openmm_martini* release[95]. A further evaluation of the OpenMM implementation of the new cholesterol model was performed by simulating DPPC:CHOL and POPC:CHOL mixtures with increasing cholesterol concentrations, and the results compared with those obtained with GROMACS. These results will be discussed in a following section, however, both MD engine implementations yielded similar results.

3.2. Cholesterol bead type assignment

Bead type assignment in cholesterol is a complex endeavor. Not only is it necessary to consider the hydrophilicity/hydrophobicity of the molecule – which dictates how it interacts with most partners – but also to consider the miscibility of cholesterol within different lipid phases – which will dictate and impact many cholesterol-dependent lipid properties. The core Martini 2 cholesterol ring consisted of type C1 beads, with the exception of the *ROH* and *R2* beads to account for the hydroxyl (type P1) and alkene (type C3) moieties. These bead types made the Martini 2 model quite miscible with saturated lipid tails (rich in C1 beads) and less so with unsaturated lipid tails (rich in C3/C4 beads). Additionally, the way that cross-interactions between regular and small beads were treated in Martini 2 – where interactions between a regular and a small bead would be treated the same as interactions between two regular beads – also improved the miscibility of the Martini 2 cholesterol with C1 beads. Altogether, this resulted in a good representation of phase separation in ternary mixtures with DPPC and DLiPC (albeit not in mixtures with DPPC and the less unsaturated DOPC). This, however, came at the expense of overestimated hydrophobicity[54] (Figure 1 f,g), which has the potential to negatively impact cholesterol interactions with other partners.

In our Martini 3 model, an effort was made to reach a compromise between overall hydrophobicity and miscibility within different lipid phases. This balance also reflects the complex structure of cholesterol, which shows both cyclic alkane and branched alkane character. The hydroxyl and double bond moieties are represented by Martini 3 P1 and C4 bead types, respectively. The sterol core (*R2, R3* and *R4*) consists of C3 beads. These beads were parameterized to be used in cyclic alkanes, and are slightly less hydrophobic than C2 and C1 bead types while maintaining good miscibility with C1. The branched groups of the model – the protruding methyl groups and the aliphatic chain (*R5, R6, C1* and *C2*) – consist of C2 beads. These were parameterized specifically to be used as branched alkanes. Indeed, the atomistic structures underlying these beads have a much higher hydrogen-to-carbon ratio than those of the sterol core. C2 beads have a higher interaction with C1 beads (which make up the Martini 3 saturated acyl chains) than their self-interaction. These beads should increase cholesterol enrichment within saturated lipid phases, which coupled with entropic packing effects, should induce favorable lipid phase separation. Indeed, the strategy of using a slightly higher cross-interaction between C2-C1 is analogous to the non-bonded fix used in the parametrization of cholesterol in CHARMM force-field[101]. In Martini 2, this effect was

included in the cross-interactions of the different bead sizes of lipid C1 tails and cholesterol SC1 beads.

Overall, this combination of C2 and C3 beads provides a better hydrophobicity landscape than the Martini 2 model, performing better in both octanol/water (within 15% of experimental reference, Figure 1 f) and hexadecane/water (within 10% of the GROMOS 54a7 theoretical reference, Figure 1 g) partitions. As seen in the following sections, this improved description of cholesterol hydrophobicity did not negatively affect the cholesterol-induced phase separation in ternary lipid bilayer systems, thus showing a good compromise between the two properties.

3.3. Cholesterol insertion and organization in lipid bilayers

3.3.1. Cholesterol insertion and flip-flop

In fully saturated lipid bilayers, the Martini 3 cholesterol is inserted in the membrane in its canonical upright orientation, with the hydroxyl group just protruding into the phosphodiester region of the bilayer (Figure 2 a), and oriented perpendicular to the bilayer plane (Supplementary Figure S3). This canonical insertion pose matches both atomistic and Martini 2 behavior, as well as experimental data on cholesterol membrane orientation[102]. By decreasing the lipid bilayer saturation, a minor population of cholesterol molecules, which transiently reside in the center of the membrane and are oriented parallel to the membrane plane, begin appearing in our Martini 3 simulations (Figure 2 a; Supplementary Figure S3). This population accounts for a very minor part of the total cholesterol content in mono-unsaturated lipid bilayers, and gradually increases with decreasing saturation, becoming the prevalent insertion pose in poly-unsaturated DAPC lipid bilayers.

Neutron scattering studies have shown that cholesterol is preferentially located in the bilayer center, parallel to the membrane plane, in poly-unsaturated lipid bilayers, namely composed of DAPC[103], as well as in cases where the extended length of a cholesterol molecule (15 Å) exceeds half the width of the acyl chain region[104]. This matches well our observation for the preferential location of our Martini 3 cholesterol model in the center of DAPC bilayers. It must be noted that experimental structural studies have only observed this non-standard location of cholesterol in these previously mentioned cases. Studies in DOPC membranes have shown that cholesterol is predominantly inserted in its canonical upright orientation (which matches the behavior we observe in our Martini 3 model); however, it is unclear whether there is room in these experimental findings for a minor population in the center of the bilayer.

The general insertion of the Martini 3 cholesterol model roughly follows the behavior of the previous Martini 2 model, with the center cholesterol population in unsaturated bilayers being slightly more prominent in the new model (Figure 2 a). For the polyunsaturated DAPC membrane, the Martini 3 model performs slightly better than in Martini 2, where the center population is expected to be dominant[103]; however, it is difficult to say whether it is overestimated in the remaining unsaturated bilayers with the existing experimental data. This effect can also be measured via flip-flop rates, which increase with decreasing saturation (Figure 2 b). The Martini 3 flip-flop rates observed were slightly increased in unsaturated bilayers when compared to Martini 2, hinting at a lower energy barrier for translocation. In saturated membrane systems, Martini 3 cholesterol flip-flop rates are in agreement with both Martini 2 and reported rates calculated from transmembrane free-energy profiles of cholesterol[105].

During the development of this model, we detected two major factors that contribute towards this population of cholesterol in the center of the membrane: i) The molecular volume of the cholesterol

model and ii) the miscibility of the cholesterol hydroxyl bead, *ROH*, within the phosphate and glycerol membrane region.

Less bulky development versions of the model showed an excessive propensity to reside in the center of the membrane. The large underlying atomistic SASA in the hydroxyl and aliphatic branching regions prompted the move to regular size beads there, instead of small. Counterintuitively, while this size change made cholesterol slightly more hydrophobic, it had a substantial impact in lowering the center plane population. This hints at the presence of a small space at the center of Martini 3 lipid membranes, likely due to insufficient interdigitation in the model or underestimated interactions between the terminal beads of each leaflet's acyl chains. As far as we know, no other reports on this have been made, but it is likely that other smaller molecules will also excessively accumulate in this region. Incidentally, the same inter-leaflet gap might already exist in Martini 2. Its influence, however, would have been mitigated by the fact that in Martini 2 interactions between small and regular size beads are the same as between regular ones.

The second factor impacting this population was the miscibility of the cholesterol hydroxyl beads within the phosphate/glycerol (PO4/GL) layer. Using a P1 bead for the hydroxyl moiety, as recommended per Martini 3 guidelines, led to slightly decreased miscibility within the PO4/GL layer compared to Martini 2. If we compare free energies of mixing between the two force field iterations, this is mostly due to decreased miscibility of Martini 3 P1 beads with SN4a and N4a glycerol beads, which seems in line with small molecule miscibility of alcohols and esters[16,50]. Increasing (P1 to P2) or decreasing (P1 to N6) the polarity of the *ROH* bead had no beneficial effect. While P2 has stronger interaction towards the phosphodiester Q5, it is even less interacting with the glycerol N4a beads. Similarly, while N6 maintains the interaction with Q5 and increases it slightly with N4a, it is also less repulsive towards the acyl chains composed of C1 beads, facilitating the ingress of cholesterol. While the overall interaction balance in Martini 3 is now better than in Martini 2, looking at the free energy of insertion of cholesterol in a POPC bilayer (Supplementary Figure S4) we do see an underestimated barrier between cholesterol *ROH* inserted at the PO4/GL depth and in the center of the membrane, when compared to both Martini 2 (~ 2 kJ/mol difference) and atomistic references (~ 15 kJ/mol difference)[105]. This explains the increase in flip flop rates in Martini 3, compared to its previous iteration. However, the ~ 30 kJ/mol discrepancy between Martini 2 and atomistic references when cholesterol is fully inserted in the center plane has now been improved in Martini 3 (~ 5 kJ/mol). Additionally, the free energy of cholesterol insertion at its equilibrium position has also been slightly improved, with a decrease in the discrepancy from ~ 20 kJ/mol in Martini 2 to ~ 10 kJ/mol in Martini 3. These improvements, while still not perfect, showcase the new model's ameliorated hydrophobicity profile, which will allow users to more easily explore cholesterol-associated features that were otherwise compromised by its overestimated hydrophobicity.

Overall, this model was developed to mitigate this issue as much as possible, while still maintaining correct interaction balances. Further ongoing development focused on the lipid models, will continue to mitigate this issue by tackling some of these factors, in particular interactions with the PO4/GL layer. These changes should lead to a slight decrease in the center plane cholesterol population through an increase in the flip-flop barrier, when coupled with future iterations of the Martini 3 lipidome.

3.3.2. Cholesterol organization

The in-plane spatial distribution of neighbors around cholesterol was also tested and compared to our atomistic reference systems (Figure 3). Our model can capture the complex asymmetric

distributions of both sterol (Figure 3 a,c,e,g) and acyl chain neighbors (Figure 3 b,d,f,h). The first neighbor acyl chain density hotspots on each specific cholesterol face are reasonably matched (Figure 3 b,d,f,h), and slightly improved compared to the Martini 2 distributions that show less structure (see Figure 5 in Melo *et al*[96]). Six interaction hotspots (Figure 3 b,d,f,h, red arrows) are observed surrounding our Martini 3 model, matching well with those observed in our AA reference. This structure is then propagated throughout the following neighbor shells, showcasing cholesterol's ability to induce lipid order. The same analysis has been previously done for the Martini 2 cholesterol model yielding only 3 interaction hotspots (see Figure 5 in Melo *et al*[96]). While the hotspot located on the smooth side of the sterol core is well modeled by both Martini 2 and Martini 3, the Martini 2 model does not accurately represent the interaction hotspots surrounding the rough cholesterol surface. The first neighbor sterol shells are substantially less clear (both in AA and Martini systems), which may hint at a slight tendency for cholesterol to avoid the first neighbor shell which is preferentially occupied by PC acyl chains (this is more clearly observed for the DPPC system, Figure 3 a,c). Instead, a more prevalent, yet less structured, second neighborhood shell appears[106]. Overall, this organization of cholesterol in lipid bilayers showcases the improved molecular shape of the model which might provide benefits not exclusive to lipid bilayers.

3.4. Impact of cholesterol on membrane bilayer systems

3.4.1. Impact of cholesterol on membrane biophysical properties

To test the impact of cholesterol on membrane bilayer systems we expanded our cholesterol-containing lipid bilayer tests and analyzed several membrane biophysical properties, such as area per lipid (APL), membrane thickness and acyl chain order for DPPC and POPC membranes containing increasing concentrations of cholesterol at 323 K. Increasing concentrations of cholesterol induced both an increase in membrane thickness and a simultaneous decrease in APL in both PC bilayers (Figure 4 a,b,d,e, Supplementary Figure S9). Regarding the magnitude of the cholesterol-induced membrane thickening (Figure 4 a,d), neutron diffraction experiments have recovered headgroup peak-to-peak distances of 44.8 Å for DPPC bilayers containing 30% cholesterol at 300 K[107], a 5.6 Å increase from pure DPPC bilayers. Running this particular system (Supplementary figure S10), we recover an increase of 3.15 and 0.61 Å for the Martini 3 and Martini 2 systems, respectively. This corresponds to a 7.46 and 1.26 % increase relative to pure lipid bilayers. Compared to the 14 % increase observed experimentally, the Martini models show insufficient thickening. However, it is clear that the new Martini 3 cholesterol model shows improved behavior compared to the previous Martini 2 iteration. AA MD simulations of POPC bilayers containing cholesterol also observed an increase in phosphate-to-phosphate thickness from 37.1 Å to 40.4 Å with the addition of 20% cholesterol at 338 K[108], compared to the 1.19 and 1.16 Å increase from our Martini 2 and Martini 3 simulations, respectively (Supplementary figure S10). In this case, both models similarly underestimate the thickening effect. While Martini 3 correctly follows the trends in bilayer thickness, we systematically underestimate the thickening effect compared to both AA MD and experimental results. This was already the case in Martini 2 (Figure 4 a,d). Still, Martini 3 performs better than Martini 2 in this aspect (especially for POPC), showcasing the improvements in both lipid and cholesterol models. This is particularly clear when looking at the percentual increase in thickness relative to pure lipid bilayers (Supplementary Figure S9), which shows that the Martini 3 model consistently yields a larger increase in thickness compared to Martini 2. It is also worth noting that a recent comparison of AA cholesterol-POPC models found an overall overestimation of the cholesterol thickening effect upon the addition of over 20% cholesterol[109]. This observation hints that the underestimation of cholesterol-induced thickening by the Martini models relative to AA references may not be as big of an issue as previously thought. Nonetheless, ongoing developments

focused on the lipid topologies and on the detail by which we represent acyl chains have the potential to further improve this feature.

Concerning the APL measurements (Figure 4 b,e), the values recovered compare well with those obtained with the CHARMM36 AA force field for both DPPC and POPC bilayers at 323 K[110]. A decrease of ~16 and ~15 Å^2 was observed in AA simulations upon the addition of 30% cholesterol to DPPC and DOPC membranes, respectively[110]. This compares well with the ~14 and ~12 Å^2 decrease observed with our Martini 3 model. Martini 2 shows a slightly stronger condensation effect in unsaturated membranes, yielding a ~14 Å^2 decrease in APL for both DPPC and POPC membranes. This small difference is likely due to the increase in the center plane cholesterol population in Martini 3, which will be decreased when coupled with future lipid models. Still, these results show similar behavior from all three models.

Experimental APL measurements show a decrease of ~14 Å^2 for SOPC (which given the nature of the 4-to-1 mapping of the Martini acyl chain beads makes it comparable to POPC) upon the addition of 28 % cholesterol at 310 K[111]. This is in line with both Martini and AA models tested here, given the known difficulties in determining APL measurements experimentally[112]. As expected from experimental results[1], cholesterol also had a very strong ordering effect in both PC bilayers (Figure 4 c,f). This ordering effect was stronger in saturated DPPC bilayers than in POPC bilayers, which required higher cholesterol concentrations to achieve substantial increases in acyl chain order. Both Martini 2 and 3 models showed identical responses in acyl chain order. Overall, these results point out that our cholesterol model is impacting simple PC bilayers well in agreement with the existing experimental and AA MD results.

This test set was also run with the OpenMM implementation of the new Martini 3 cholesterol model (Supplementary Figure S8), replicating the conditions of the same simulations run in GROMACS. Our results show a dependence of membrane thickness, APL, and acyl chain order with increasing cholesterol concentration, in a manner that is consistent with results obtained in GROMACS simulations, further validating the OpenMM implementation.

3.4.2. Impact of cholesterol on the phase behavior of binary and ternary lipid membranes

We also tested the impact of cholesterol on phase separation. We started by probing two specific conditions of the DPPC:CHOL binary phase diagram at 300 K. At 15 mol% cholesterol, DPPC bilayers remain fully in a gel phase, with the cholesterol molecules frozen within the hexagonal gel matrix (Supplementary Figure S5). At 30 mol%, cholesterol can fluidify the gel matrix into an Lo phase where we observe the transient formation of small gel-like DPPC domains. Coexistence with these small domains is quite dynamic, with the gel domains assembling and then quickly dissolving after a few nanoseconds (Supplementary Video S1). Whether these transient gel-like domains are nucleation points for the formation of a larger gel-phase or gel-like substructure elements of the Lo phase that may exist at this temperature[113–115], this observation is already a promising improvement over Martini 2 which struggled to show any such structures[23]. Experimental DPPC:CHOL binary phase studies conducted at 295-300 K[116–122] predict the gel to Lo/Gel transition to occur anywhere between 3 to 20 mol% cholesterol, with the following Lo/Gel to Lo transition occurring between 20 and 30 mol% cholesterol. The uncertainty in defining the transition boundaries is likely due to the intrinsic resolution and sensitivity limitations of the experimental methods used in probing these dynamic local domains in a membrane environment[122]. Nonetheless, our results reasonably match experimental observations. Note that given the nature of the 4-to-1 mapping of the Martini acyl chain beads, the Martini 3 DPPC represents both $(16:0)_2$ and $(18:0)_2$ PC lipids (i.e. DPPC and DSPC).

DSPC can tolerate higher mol% of cholesterol before a phase transition happens[116,119], which could skew Martini 3 results towards requiring slightly higher cholesterol concentrations.

We also tested the phase separation of ternary systems composed of DPPC, an unsaturated PC lipid (DLiPC, DOPC) and cholesterol at 42:28:30 mol% ratios and at both 300 and 290 K (Figure 5). The DPPC:DLiPC:CHOL system phase separated, inducing the formation of a more ordered DPPC-rich phase containing the large majority of cholesterol incorporated within it, and a more fluid DLiPC phase (Figure 5 a,c,e,g,i,j). This phase separation occurs at both 290 and 300 K, and is in good agreement with both Martini 2 and experimental results[116,123].

When replacing DLiPC with the more saturated DOPC, phase separation becomes substantially less clear, with more mixing between DOPC and DPPC as well as a decrease in the enrichment of cholesterol-DPPC contacts (Figure 5 b,d,f,h,i,j). No clear phase separation is observed at either 290 or 300 K. Experimental data points out that a single uniform phase should be obtained for DPPC:DOPC:CHOL at 300 K[116,123], but coexistence of Lo and Ld phases should be observed at 290 K[116,123]. It is not clear how much our cholesterol model is impacting phase separation in this ternary model and whether there is much room for improvement, especially since the underlying DOPC:DPPC and POPC:DPPC binary mixtures also fail to show correct phase separation with the current Martini 3 lipid model[124]. If we compare the specific contact fractions calculated from the both Martini 3 and 2 systems (Figure 5 i,j), we already observe a small improvement in the enrichment of DPPC-DPPC and DPPC-CHOL contacts with the newer model. These results hint at a slightly improved propensity to phase separate. Further developments focused on the lipid models will likely fix these ternary models, by improving the underlying DPPC:DOPC binary mixtures[124]. Moreover, it is worth noting that these results were obtained without the temperature differences arising from LINCS convergence and influencing the degree of phase separation[55]. Indeed, the Martini 2 model phase separation was in part due to these issues, while our model can achieve similar levels of separation without this artifact.

Atomistic studies on phase-separating DPPC:DOPC:CHOL ternary mixtures have shown a peculiar organization of cholesterol, with the cholesterol methyl-protruding face maximizing contacts with DOPC, while the smooth cholesterol face maximizing DPPC contacts[125]. At lower temperatures (~270-280 K), these segregate to the boundaries of the two phases. We do not see evidence of this complex organization in any of our Martini 3 or 2 phase-separating systems. However, with Martini 3, much like with the DPPC:CHOL binary mixtures, some highly ordered gel-like substructures were observed within the DPPC-rich Lo phases, in line with experimental and AA findings[113–115]. No such substructures are observed with Martini 2.

3.6 Cholesterol crystal packing

The packing of the new cholesterol model in the crystal structures of pure cholesterol (CCDC code: CHOEST20) and cholesterol monohydrate (CCDC code: CHOLES20) was also tested. Supplementary Figure S7 shows the CG crystal structures as well as the averaged structures of 200 ns of CG simulation at 200 K. The increase in disorder is more pronounced for the cholesterol monohydrate than for pure cholesterol. An increase in disorder compared to the atomistic structures is to be expected due to the smoothened molecular surface (Fig. 1b). The higher disorder in the monohydrate could be explained by the smoothened spherical surface of the tiny TW bead and a slight size mismatch compared to a water molecule. The introduced harmonic bonds to mimic the hydrogen bonds cannot fully compensate for the loss of molecular symmetry. Table 1 shows the changes of the unit cells for the CG structure of CHOEST20 compared to experiment. The simulated unit cells deviate by 0–7% of the box vector length. While the box vectors a and b are slightly smaller

or larger than the experimental ones, c is smaller by 7% at 200 K and 6% at 295 K, respectively. The absolute changes are also most pronounced for c. Overall, the unit cell volume decreases by 5–6%. For cholesterol monohydrate, the changes of the three box vectors are comparable to the ones of the pure cholesterol structure (Table 1). While a shrinking by 2% and 11% at 200 K and 295 K, respectively, b and c increase by 1–6% except for b at 200 K which slightly decreases. The unit cell volume shrinks by 2% at 200 K and by less than 1% at 295 K, respectively. In summary, the crystal structure simulations confirm the well reproduced shape and packing of the new Martini 3 cholesterol model.

Table 1. Cholesterol crystal structures. Unit cell parameters for CG simulations of the crystal structures of cholesterol CHOEST20 and cholesterol monohydrate CHOLES20 compared to experiment. All statistical errors of the simulated data are below 0.001 nm, 0.004° and 0.001 nm^3, respectively.

	Cholesterol CHOEST20			Cholesterol monohydrate CHOLES20		
	CG Martini 3		exp.	CG Martini 3		exp.
T / K	200	295	295	200	295	295
a / nm	1.39	1.43	1.41	1.22	1.11	1.24
b / nm	3.52	3.42	3.42	1.22	1.31	1.24
c / nm	0.98	0.99	1.05	3.49	3.60	3.44
α / °	95.11	94.91	94.64	91.66	91.94	91.91
β / °	90.71	90.72	90.67	98.14	97.64	98.11
γ / °	96.01	96.46	96.32	101.20	100.10	100.81
V / nm^3	4.74	4.80	5.03	5.05	5.12	5.13

3.5. Cholesterol-protein interactions

Cholesterol-protein interactions are fundamental both for the correct organization of biological membranes, as well as for cellular homeostasis. With this in mind, our model must correctly replicate known interaction behavior. To test this, we probed the recognition and binding of our cholesterol model by 3 cholesterol-binding proteins: the human β_2-adrenergic receptor (β_2AR), the transmembrane domain of the hedgehog signal transducer and class F G protein-coupled receptor (GPCR) smoothened (SMO), and the voltage-dependent anion channel 1 (VDAC1). These 3

selected proteins showcase well the typical cholesterol-protein interactions which are usually explored using Martini and include extensive reference data for validation[25,126].

The β_2AR is a class A GPCR associated with the downstream regulation of L-type calcium channels and subsequent modulation of physiological responses such as relaxation of smooth muscle, bronchodilation, glycogenolysis, and gluconeogenesis. It is also involved in the regulation of the cell metabolism in skeletal muscle in response to noradrenaline and adrenaline[127–129]. X-Ray crystallographic data from multiple sources show two clear cholesterol interaction sites between helices 1 and 4[87,130,131] as well as between helices 1 and 7[130,131] (Figure 6 a). For convenience, we labeled this interaction site as binding site 1. Cholesterol interaction in this site is also observed in atomistic MD studies of β_2AR[132–134]. Our Martini 3 cholesterol model recovers binding at this interaction site with high residence time, in agreement with the existing references (Figure 6 a, b, c). Our model also interacts with other interaction sites across the β_2AR surface (Figure 6 c): binding site 2 between helices 4 and 5; binding site 3 between helices 5 and 6; and binding site 4 between helices 6 and 7. These interaction sites have also been observed in atomistic MD studies[132–134].

The SMO receptor is a class F GPCR and a vital component of the Hedgehog signaling cascade responsible for embryonic development and the regulation of adult stem cells[84]. Like β_2AR and other GPCRs, it is suggested that SMO is regulated via interactions of its transmembrane domain with cholesterol. A study by Hedger et al. has recently identified a cholesterol interaction site using a multiscale MD approach that combined Martini 2 and GROMOS53a6[84]. This interaction site is located on the transmembrane domain of SMO at the extracellular tips of helices H2 and H3 (Figure 7 a). Our model recognized this interaction site (BS1) on the surface of SMO (Figure 7 a, b, and c) in agreement with the findings of Hedger *et al.*[84]. A second interaction site (BS2) was also observed between H1 and H7 (Figure 7 a, b, and d) with similar residence time as the one described by Hedger *et al.* [84]

VDAC1 is a voltage-dependent anion channel with a number of binding sites for cholesterol. It is responsible for the regulation of ion and metabolite flux between the cytosol and the mitochondrial intermembrane space[86]. Several theoretical and experimental studies have identified numerous cholesterol interaction sites on the transmembrane surface of VDAC1. Our Martini 3 cholesterol model binds to VDAC1 via 3 distinct binding sites (Supplementary Figure S6). Binding sites 1 and 2 match well with some of the cholesterol-binding sites detected with docking procedures (BS1 with DS1, BS2 with DS4, and BS3 with DS5)[135]. The three binding sites are also in rough agreement with those detected on the surface of VDAC1 using Martini 2[86]. It is worth noting that we did not detect significant cholesterol occupancy on some of the binding sites predicted by docking, namely DS2 and DS3[135]. These were also not significantly populated by the previous Martini 2 model[86]. Finally, binding site 3, the binding site with higher residence time detected, is well in agreement with a cholesterol-binding site detected by photo-affinity labeling experiments[136,137].

Overall, the recognition and binding behavior observed with these representative proteins show that the Martini 3 cholesterol model is correctly interacting with proteins and replicating both experimental and theoretical references. For users comparing the results obtained with the previous Martini 2 model with the current Martini 3 cholesterol, it is important to account for the overall stickiness of the Martini 2 model[43]. Molecules in Martini 2 were found to be too hydrophobic or self-interact too strongly, particularly when mappings finer than 4-to-1 were employed. This impacted both proteins and possibly cholesterol, and as such, it is to be expected that Martini 3 protein-cholesterol interactions are more transient in nature than the Martini 2 counterparts. Indeed the cholesterol residence times calculated for our test cases were in the 80-100 nanosecond timescale, while in Martini 2 the typical cholesterol residence time would likely be in the microsecond timescale.

Compared to existing AA data our residence times are potentially underestimated. Two out of three 200 ns AA (GROMOS53a6) simulations of cholesterol bound to the SMO receptor BS1 site showed partial dissociation and reorientation[84]. While this is not enough sampling to calculate an average residence time, it hints at times similar to the ~80 ns we recover for this site. AA (CHARMM27 protein model with CHARMM35 cholesterol) simulations of β_2AR show residence times ranging from 100 ns up to several microseconds[133,138]. In this case, Martini 3 underestimates the residence times observed. Importantly, for both proteins we still recover similarly high levels of occupancy as a result of rapid exchange events between multiple cholesterol molecules.

It is important to note that kinetic processes in Martini, such as the binding and unbinding of cholesterol, are not always correctly recovered. If a process is dominated by enthalpic contributions, such as in the case of cholesterol flip-flop, Martini should recover reasonable kinetics. However, in entropy dominated processes, such as in diffusional-based mechanisms, the kinetics are often substantially sped up due to the missing atomistic degrees of freedom. While the binding/unbinding of cholesterol to a protein in a membrane context, has a non-negligible enthalpic contribution (enthalpic competition between cholesterol and lipid acyl chains for the binding site), it also has a substantial entropic contribution (cholesterol diffusion in and out of the binding site, side-chain reorientation) which will be sped up in Martini. It must also be mentioned that residency times vary substantially due to system setup (force field, temperature, Chol mol%, lipid composition, etc.) and the analysis method used. One last aspect that could potentially impact cholesterol binding, is the overall hydrophobicity of the protein model. Growing evidence hints that the Martini 3 protein model may be too hydrophilic[139–141], as seen by typical transmembrane peptides being ejected to the membrane periphery. If this is the case, it is likely that interactions with hydrophobic molecules, such as cholesterol, may be slightly impacted. Nonetheless, with enough sampling, interaction sites are expected to remain mostly consistent between Martini 3 and Martini 2 and in agreement with AA data, albeit with more dynamic interactions.

4. Conclusion

In this work, we successfully develop and validate a Martini 3 CG model of cholesterol. Our goal with this effort was not just to revisit and update the previous model[96] to the Martini 3 framework[16], but also to address issues pertaining to the previous model. A compromise was made to address some of these points while maintaining or improving the characteristics of the previous model as much as possible. A more refined description of the mapping and bead types led to an improved hydrophobicity and interaction landscape, refining cholesterol interactions with other partners and reducing possible model stickiness. Cholesterol shape and volume were improved, yielding better packing in lipid bilayers and good crystal packing. The artificial temperature gradients due to convergence issues with the LINCS algorithm were solved while maintaining phase separation properties in line with the Martini 2 model and experimental data. Overall, this model is another step in the evolution of the already successful Martini 2 cholesterol model. We foresee iterative improvements in both the Martini 3 phospholipid models and the interaction matrix in the near future, which should impact in a more accurate description of phase diagrams of ternary mixtures like DPPC:DOPC:CHOL.

Acknowledgements

We would like to acknowledge all users of the molecular modeling community that tested beta versions of the cholesterol model, in particular the feedback from Lorena Zuzic, Lisbeth Ravnkilde Kjølbye, Mikkel Dahl Andreasen, Gilberto Pereira, Nathalie Reuter, Reza Talandashti, Changjin

Huang, Choon-Peng, Christina Athanasiou, Azadeh Alavizargar, Amita Sahoo, Matthias Buck, Syma Khalid, Jeroen Methorst, Herre Jelger Risselada, Alessandro Marchetto, Simone Albani and Giulia Rossetti. M.N.M. acknowledges financial support from Fundação para a Ciência e a Tecnologia (fellowship CEECIND/04124/2017 and project MOSTMICRO-ITQB, with references UIDB/04612/2020 and UIDP/04612/2020). L.B.A. and P.C.T.S acknowledge the computer time on the Jean-Zay and Joliot-Curie Rome clusters of the French National Supercomputing Center (GENCI project number 2022/A0120713456). L.B.A. and P.C.T.S also acknowledge the support provided by the CNRS and PharmCADD. B.F. thanks the Alexander von Humboldt-Foundation for funding. B.F. and G.H. thank the Max Planck Society for support. S.T. acknowledges access to the HPC clusters FUCHS and GoetheHLR provided by the Center for Scientific Computing at the Goethe University Frankfurt. S.T. thanks the Hessian Ministry of Science and Arts LOEWE program (Center for Multiscale Modeling in Life Sciences, CMMS), the Alfons und Gertrud Kassel foundation, and Dr. Rolf M. Schwiete foundation for funding. S.J.M. acknowledges ERC funding (grant agreement no. 101053661 - COMP-O-CELL). D.P.T. acknowledges support from the Natural Sciences and Engineering Research Council (Canada), the Canada Research Chairs Program, and the Digital Research Alliance of Canada. T.N.O., T.S.C and H.I.I. thank the Livermore Institutional Grand Challenge for computing time and LDRD 21-ERD-047 for funding. Part of this work performed under the auspices of the U.S. Department of Energy by Lawrence Livermore National Laboratory under Contract DE-AC52-07NA27344, LLNL-JRNL-854111.

Associated content

Supporting Document: contains extended descriptions of system setup, model topology, and analysis methods, as well as results from additional simulations and measurements. *Supporting Video S1*: Last 500 ns of the top view of membrane simulations of Martini 3 70:30 DPPC:CHOL, 85:15 DPPC:CHOL and 85:15 DOPC:CHOL, at 300 K. DPPC first acyl-chain beads (C1A, C1B) are represented in grey. Cholesterol hydroxyl bead (ROH) is represented in red.

References

(1) Subczynski, W. K.; Pasenkiewicz-Gierula, M.; Widomska, J.; Mainali, L.; Raguz, M. High Cholesterol/Low Cholesterol: Effects in Biological Membranes: A Review. *Cell Biochem. Biophys.* **2017**, *75* (3–4), 369–385. https://doi.org/10.1007/s12013-017-0792-7.

(2) Nelson, D. L.; Cox, M. M. *Lehninger Principles of Biochemistry*, 7th ed.; W.H. Freeman: New York.

(3) Marsh, D. Liquid-Ordered Phases Induced by Cholesterol: A Compendium of Binary Phase Diagrams. *Biochim. Biophys. Acta BBA - Biomembr.* **2010**, *1798* (3), 688–699. https://doi.org/10.1016/j.bbamem.2009.12.027.

(4) Levental, I.; Levental, K. R.; Heberle, F. A. Lipid Rafts: Controversies Resolved, Mysteries Remain. *Trends Cell Biol.* **2020**, *30* (5), 341–353. https://doi.org/10.1016/j.tcb.2020.01.009.

(5) Fantini, J.; Barrantes, F. How Cholesterol Interacts with Membrane Proteins: An Exploration of Cholesterol-Binding Sites Including CRAC, CARC, and Tilted Domains. *Front. Physiol.* **2013**, *4*.

(6) Bukiya, A. N.; Dopico, A. M. Common Structural Features of Cholesterol Binding Sites in Crystallized Soluble Proteins. *J. Lipid Res.* **2017**, *58* (6), 1044–1054. https://doi.org/10.1194/jlr.R073452.

(7) Pozzi, D.; Marchini, C.; Cardarelli, F.; Amenitsch, H.; Garulli, C.; Bifone, A.; Caracciolo, G. Transfection Efficiency Boost of Cholesterol-Containing Lipoplexes. *Biochim. Biophys. Acta BBA - Biomembr.* **2012**, *1818* (9), 2335–2343. https://doi.org/10.1016/j.bbamem.2012.05.017.

(8) Hald Albertsen, C.; Kulkarni, J. A.; Witzigmann, D.; Lind, M.; Petersson, K.; Simonsen, J. B.

The Role of Lipid Components in Lipid Nanoparticles for Vaccines and Gene Therapy. *Adv. Drug Deliv. Rev.* **2022**, *188*, 114416. https://doi.org/10.1016/j.addr.2022.114416.
(9) Marrink, S. J.; Corradi, V.; Souza, P. C. T.; Ingólfsson, H. I.; Tieleman, D. P.; Sansom, M. S. P. Computational Modeling of Realistic Cell Membranes. *Chem. Rev.* **2019**, *119* (9), 6184–6226. https://doi.org/10.1021/acs.chemrev.8b00460.
(10) Venable, R. M.; Krämer, A.; Pastor, R. W. Molecular Dynamics Simulations of Membrane Permeability. *Chem. Rev.* **2019**, *119* (9), 5954–5997. https://doi.org/10.1021/acs.chemrev.8b00486.
(11) Moradi, S.; Nowroozi, A.; Shahlaei, M. Shedding Light on the Structural Properties of Lipid Bilayers Using Molecular Dynamics Simulation: A Review Study. *RSC Adv.* **2019**, *9* (8), 4644–4658. https://doi.org/10.1039/C8RA08441F.
(12) Corradi, V.; Mendez-Villuendas, E.; Ingólfsson, H. I.; Gu, R.-X.; Siuda, I.; Melo, M. N.; Moussatova, A.; DeGagné, L. J.; Sejdiu, B. I.; Singh, G.; Wassenaar, T. A.; Delgado Magnero, K.; Marrink, S. J.; Tieleman, D. P. Lipid–Protein Interactions Are Unique Fingerprints for Membrane Proteins. *ACS Cent. Sci.* **2018**, *4* (6), 709–717. https://doi.org/10.1021/acscentsci.8b00143.
(13) Larsen, A. H. Molecular Dynamics Simulations of Curved Lipid Membranes. *Int. J. Mol. Sci.* **2022**, *23* (15), 8098. https://doi.org/10.3390/ijms23158098.
(14) Muller, M. P.; Jiang, T.; Sun, C.; Lihan, M.; Pant, S.; Mahinthichaichan, P.; Trifan, A.; Tajkhorshid, E. Characterization of Lipid–Protein Interactions and Lipid-Mediated Modulation of Membrane Protein Function through Molecular Simulation. *Chem. Rev.* **2019**, *119* (9), 6086–6161. https://doi.org/10.1021/acs.chemrev.8b00608.
(15) Ingólfsson, H. I.; Arnarez, C.; Periole, X.; Marrink, S. J. Computational 'Microscopy' of Cellular Membranes. *J. Cell Sci.* **2016**, jcs.176040. https://doi.org/10.1242/jcs.176040.
(16) Souza, P. C. T.; Alessandri, R.; Barnoud, J.; Thallmair, S.; Faustino, I.; Grünewald, F.; Patmanidis, I.; Abdizadeh, H.; Bruininks, B. M. H.; Wassenaar, T. A.; Kroon, P. C.; Melcr, J.; Nieto, V.; Corradi, V.; Khan, H. M.; Domański, J.; Javanainen, M.; Martinez-Seara, H.; Reuter, N.; Best, R. B.; Vattulainen, I.; Monticelli, L.; Periole, X.; Tieleman, D. P.; de Vries, A. H.; Marrink, S. J. Martini 3: A General Purpose Force Field for Coarse-Grained Molecular Dynamics. *Nat. Methods* **2021**, *18* (4), 382–388. https://doi.org/10.1038/s41592-021-01098-3.
(17) Marrink, S. J.; Risselada, H. J.; Yefimov, S.; Tieleman, D. P.; de Vries, A. H. The MARTINI Force Field: Coarse Grained Model for Biomolecular Simulations. *J. Phys. Chem. B* **2007**, *111* (27), 7812–7824. https://doi.org/10.1021/jp071097f.
(18) Arnarez, C.; Webb, A.; Rouvière, E.; Lyman, E. Hysteresis and the Cholesterol Dependent Phase Transition in Binary Lipid Mixtures with the Martini Model. *J. Phys. Chem. B* **2016**, *120* (51), 13086–13093. https://doi.org/10.1021/acs.jpcb.6b09728.
(19) Ackerman, D. G.; Feigenson, G. W. Multiscale Modeling of Four-Component Lipid Mixtures: Domain Composition, Size, Alignment, and Properties of the Phase Interface. *J. Phys. Chem. B* **2015**, *119* (11), 4240–4250. https://doi.org/10.1021/jp511083z.
(20) Wang, Y.; Gkeka, P.; Fuchs, J. E.; Liedl, K. R.; Cournia, Z. DPPC-Cholesterol Phase Diagram Using Coarse-Grained Molecular Dynamics Simulations. *Biochim. Biophys. Acta* **2016**, *1858* (11), 2846–2857. https://doi.org/10.1016/j.bbamem.2016.08.005.
(21) He, S.; Maibaum, L. Identifying the Onset of Phase Separation in Quaternary Lipid Bilayer Systems from Coarse-Grained Simulations. *J. Phys. Chem. B* **2018**, *122* (14), 3961–3973. https://doi.org/10.1021/acs.jpcb.8b00364.
(22) Podewitz, M.; Wang, Y.; Gkeka, P.; von Grafenstein, S.; Liedl, K. R.; Cournia, Z. Phase Diagram of a Stratum Corneum Lipid Mixture. *J. Phys. Chem. B* **2018**, *122* (46), 10505–10521. https://doi.org/10.1021/acs.jpcb.8b07200.
(23) Carpenter, T. S.; López, C. A.; Neale, C.; Montour, C.; Ingólfsson, H. I.; Di Natale, F.; Lightstone, F. C.; Gnanakaran, S. Capturing Phase Behavior of Ternary Lipid Mixtures with a Refined Martini Coarse-Grained Force Field. *J. Chem. Theory Comput.* **2018**, *14* (11), 6050–6062. https://doi.org/10.1021/acs.jctc.8b00496.
(24) Pantelopulos, G. A.; Straub, J. E. Regimes of Complex Lipid Bilayer Phases Induced by Cholesterol Concentration in MD Simulation. *Biophys. J.* **2018**, *115* (11), 2167–2178. https://doi.org/10.1016/j.bpj.2018.10.011.
(25) Corradi, V.; Sejdiu, B. I.; Mesa-Galloso, H.; Abdizadeh, H.; Noskov, S. Yu.; Marrink, S. J.;

Tieleman, D. P. Emerging Diversity in Lipid–Protein Interactions. *Chem. Rev.* **2019**, *119* (9), 5775–5848. https://doi.org/10.1021/acs.chemrev.8b00451.
(26) Travers, T.; López, C. A.; Van, Q. N.; Neale, C.; Tonelli, M.; Stephen, A. G.; Gnanakaran, S. Molecular Recognition of RAS/RAF Complex at the Membrane: Role of RAF Cysteine-Rich Domain. *Sci. Rep.* **2018**, *8* (1), 8461. https://doi.org/10.1038/s41598-018-26832-4.
(27) Hall, B. A.; Armitage, J. P.; Sansom, M. S. P. Mechanism of Bacterial Signal Transduction Revealed by Molecular Dynamics of Tsr Dimers and Trimers of Dimers in Lipid Vesicles. *PLOS Comput. Biol.* **2012**, *8* (9), e1002685. https://doi.org/10.1371/journal.pcbi.1002685.
(28) Chng, C.-P.; Tan, S.-M. Leukocyte Integrin αLβ2 Transmembrane Association Dynamics Revealed by Coarse-Grained Molecular Dynamics Simulations. *Proteins* **2011**, *79* (7), 2203–2213. https://doi.org/10.1002/prot.23044.
(29) Prakash, A.; Janosi, L.; Doxastakis, M. GxxxG Motifs, Phenylalanine, and Cholesterol Guide the Self-Association of Transmembrane Domains of ErbB2 Receptors. *Biophys. J.* **2011**, *101* (8), 1949–1958. https://doi.org/10.1016/j.bpj.2011.09.017.
(30) Faustino, I.; Abdizadeh, H.; Souza, P. C. T.; Jeucken, A.; Stanek, W. K.; Guskov, A.; Slotboom, D. J.; Marrink, S. J. Membrane Mediated Toppling Mechanism of the Folate Energy Coupling Factor Transporter. *Nat. Commun.* **2020**, *11* (1), 1763. https://doi.org/10.1038/s41467-020-15554-9.
(31) Bruininks, B. M.; Souza, P. C.; Ingolfsson, H.; Marrink, S. J. A Molecular View on the Escape of Lipoplexed DNA from the Endosome. *eLife* **2020**, *9*, e52012. https://doi.org/10.7554/eLife.52012.
(32) Markvoort, A. J.; Marrink, S. J. Chapter 11 - Lipid Acrobatics in the Membrane Fusion Arena. In *Current Topics in Membranes*; Chernomordik, L. V., Kozlov, M. M., Eds.; Academic Press, 2011; Vol. 68, pp 259–294. https://doi.org/10.1016/B978-0-12-385891-7.00011-8.
(33) Smirnova, Y. G.; Risselada, H. J.; Müller, M. Thermodynamically Reversible Paths of the First Fusion Intermediate Reveal an Important Role for Membrane Anchors of Fusion Proteins. *Proc. Natl. Acad. Sci.* **2019**, *116* (7), 2571–2576. https://doi.org/10.1073/pnas.1818200116.
(34) Pannuzzo, M.; De Jong, D. H.; Raudino, A.; Marrink, S. J. Simulation of Polyethylene Glycol and Calcium-Mediated Membrane Fusion. *J. Chem. Phys.* **2014**, *140* (12), 124905. https://doi.org/10.1063/1.4869176.
(35) Risselada, H. J.; Marrink, S. J. Curvature Effects on Lipid Packing and Dynamics in Liposomes Revealed by Coarse Grained Molecular Dynamics Simulations. *Phys. Chem. Chem. Phys.* **2009**, *11* (12), 2056–2067. https://doi.org/10.1039/B818782G.
(36) Risselada, H. J.; Marrink, S. J.; Müller, M. Curvature-Dependent Elastic Properties of Liquid-Ordered Domains Result in Inverted Domain Sorting on Uniaxially Compressed Vesicles. *Phys. Rev. Lett.* **2011**, *106* (14), 148102. https://doi.org/10.1103/PhysRevLett.106.148102.
(37) Baoukina, S.; Ingólfsson, H. I.; Marrink, S. J.; Tieleman, D. P. Curvature-Induced Sorting of Lipids in Plasma Membrane Tethers. *Adv. Theory Simul.* **2018**, *1* (8), 1800034. https://doi.org/10.1002/adts.201800034.
(38) Pezeshkian, W.; Marrink, S. J. Simulating Realistic Membrane Shapes. *Curr. Opin. Cell Biol.* **2021**, *71*, 103–111. https://doi.org/10.1016/j.ceb.2021.02.009.
(39) De Franceschi, N.; Pezeshkian, W.; Fragasso, A.; Bruininks, B. M. H.; Tsai, S.; Marrink, S. J.; Dekker, C. Synthetic Membrane Shaper for Controlled Liposome Deformation. *ACS Nano* **2022**, *17* (2), 966–978. https://doi.org/10.1021/acsnano.2c06125.
(40) Ingólfsson, H. I.; Melo, M. N.; van Eerden, F. J.; Arnarez, C.; Lopez, C. A.; Wassenaar, T. A.; Periole, X.; de Vries, A. H.; Tieleman, D. P.; Marrink, S. J. Lipid Organization of the Plasma Membrane. *J. Am. Chem. Soc.* **2014**, *136* (41), 14554–14559. https://doi.org/10.1021/ja507832e.
(41) Ingólfsson, H. I.; Carpenter, T. S.; Bhatia, H.; Bremer, P.-T.; Marrink, S. J.; Lightstone, F. C. Computational Lipidomics of the Neuronal Plasma Membrane. *Biophys. J.* **2017**, *113* (10), 2271–2280. https://doi.org/10.1016/j.bpj.2017.10.017.
(42) Marrink, S. J.; Monticelli, L.; Melo, M. N.; Alessandri, R.; Tieleman, D. P.; Souza, P. C. T. Two Decades of Martini: Better Beads, Broader Scope. *WIREs Comput Mol Sci* **2022**, e1620.
(43) Alessandri, R.; Souza, P. C. T.; Thallmair, S.; Melo, M. N.; de Vries, A. H.; Marrink, S. J. Pitfalls of the Martini Model. *J. Chem. Theory Comput.* **2019**, *15* (10), 5448–5460.

https://doi.org/10.1021/acs.jctc.9b00473.
(44) Stark, A. C.; Andrews, C. T.; Elcock, A. H. Toward Optimized Potential Functions for Protein–Protein Interactions in Aqueous Solutions: Osmotic Second Virial Coefficient Calculations Using the MARTINI Coarse-Grained Force Field. *J. Chem. Theory Comput.* **2013**, *9* (9), 4176–4185. https://doi.org/10.1021/ct400008p.
(45) Javanainen, M.; Martinez-Seara, H.; Vattulainen, I. Excessive Aggregation of Membrane Proteins in the Martini Model. *PLOS ONE* **2017**, *12* (11), e0187936. https://doi.org/10.1371/journal.pone.0187936.
(46) Schmalhorst, P. S.; Deluweit, F.; Scherrers, R.; Heisenberg, C.-P.; Sikora, M. Overcoming the Limitations of the MARTINI Force Field in Simulations of Polysaccharides. *J. Chem. Theory Comput.* **2017**, *13* (10), 5039–5053. https://doi.org/10.1021/acs.jctc.7b00374.
(47) Borges-Araújo, L.; Souza, P. C. T.; Fernandes, F.; Melo, M. N. Improved Parameterization of Phosphatidylinositide Lipid Headgroups for the Martini 3 Coarse-Grain Force Field. *J. Chem. Theory Comput.* **2022**, *18* (1), 357–373. https://doi.org/10.1021/acs.jctc.1c00615.
(48) Grünewald, F.; Punt, M. H.; Jefferys, E. E.; Vainikka, P. A.; König, M.; Virtanen, V.; Meyer, T. A.; Pezeshkian, W.; Gormley, A. J.; Karonen, M.; Sansom, M. S. P.; Souza, P. C. T.; Marrink, S. J. Martini 3 Coarse-Grained Force Field for Carbohydrates. *J. Chem. Theory Comput.* **2022**, acs.jctc.2c00757. https://doi.org/10.1021/acs.jctc.2c00757.
(49) Lutsyk, V.; Wolski, P.; Plazinski, W. Extending the Martini 3 Coarse-Grained Force Field to Carbohydrates. *J. Chem. Theory Comput.* **2022**, *18* (8), 5089–5107. https://doi.org/10.1021/acs.jctc.2c00553.
(50) Alessandri, R.; Barnoud, J.; Gertsen, A. S.; Patmanidis, I.; de Vries, A. H.; Souza, P. C. T.; Marrink, S. J. Martini 3 Coarse-Grained Force Field: Small Molecules. *Adv. Theory Simul.* **2022**, *5* (1), 2100391. https://doi.org/10.1002/adts.202100391.
(51) Vainikka, P.; Thallmair, S.; Souza, P. C. T.; Marrink, S. J. Martini 3 Coarse-Grained Model for Type III Deep Eutectic Solvents: Thermodynamic, Structural, and Extraction Properties. *ACS Sustain. Chem. Eng.* **2021**, *9* (51), 17338–17350. https://doi.org/10.1021/acssuschemeng.1c06521.
(52) Vazquez-Salazar, L. I.; Selle, M.; Vries, A. H. de; Marrink, S. J.; Souza, P. C. T. Martini Coarse-Grained Models of Imidazolium-Based Ionic Liquids: From Nanostructural Organization to Liquid–Liquid Extraction. *Green Chem.* **2020**, *22* (21), 7376–7386. https://doi.org/10.1039/D0GC01823F.
(53) Hilpert, C.; Beranger, L.; Souza, P. C. T.; Vainikka, P. A.; Nieto, V.; Marrink, S. J.; Monticelli, L.; Launay, G. Facilitating CG Simulations with MAD: The MArtini Database Server. *J. Chem. Inf. Model.* **2023**, *63* (3), 702–710. https://doi.org/10.1021/acs.jcim.2c01375.
(54) Fornasier, F.; Souza, L. M. P.; Souza, F. R.; Reynaud, F.; Pimentel, A. S. Lipophilicity of Coarse-Grained Cholesterol Models. *J. Chem. Inf. Model.* **2020**, *60* (2), 569–577. https://doi.org/10.1021/acs.jcim.9b00830.
(55) Thallmair, S.; Javanainen, M.; Fábián, B.; Martinez-Seara, H.; Marrink, S. J. Nonconverged Constraints Cause Artificial Temperature Gradients in Lipid Bilayer Simulations. *J. Phys. Chem. B* **2021**, *125* (33), 9537–9546. https://doi.org/10.1021/acs.jpcb.1c03665.
(56) Fábián, B.; Thallmair, S.; Hummer, G. Optimal Bond Constraint Topology for Molecular Dynamics Simulations of Cholesterol. *J. Chem. Theory Comput.* **2023**, *19* (5), 1592–1601. https://doi.org/10.1021/acs.jctc.2c01032.
(57) Abraham, M.; Murtola, T.; Schulz, R.; Páll, S.; Smith, J.; Hess, B.; Lindahl, E. GROMACS: High Performance Molecular Simulations through Multi-Level Parallelism from Laptops to Supercomputers. *SoftwareX* **2015**, *1*. https://doi.org/10.1016/j.softx.2015.06.001.
(58) Michaud-Agrawal, N.; Denning, E. J.; Woolf, T. B.; Beckstein, O. MDAnalysis: A Toolkit for the Analysis of Molecular Dynamics Simulations. *J. Comput. Chem.* **2011**, *32* (10), 2319–2327. https://doi.org/10.1002/jcc.21787.
(59) Gowers, R. J.; Linke, M.; Barnoud, J.; Reddy, T. J. E.; Melo, M. N.; Seyler, S. L.; Domanski, J.; Dotson, D. L.; Buchoux, S.; Kenney, I. M.; Beckstein, O. *MDAnalysis: A Python Package for the Rapid Analysis of Molecular Dynamics Simulations*; LA-UR-19-29136; Los Alamos National Lab. (LANL), Los Alamos, NM (United States), 2019. https://doi.org/10.25080/Majora-629e541a-00e.
(60) Perez, F.; Granger, B. IPython: A System for Interactive Scientific Computing. *Comput. Sci. Eng.* **2007**, *9*, 21–29. https://doi.org/10.1109/MCSE.2007.53.

(61) Harris, C. R.; Millman, K. J.; van der Walt, S. J.; Gommers, R.; Virtanen, P.; Cournapeau, D.; Wieser, E.; Taylor, J.; Berg, S.; Smith, N. J.; Kern, R.; Picus, M.; Hoyer, S.; van Kerkwijk, M. H.; Brett, M.; Haldane, A.; Del Río, J. F.; Wiebe, M.; Peterson, P.; Gérard-Marchant, P.; Sheppard, K.; Reddy, T.; Weckesser, W.; Abbasi, H.; Gohlke, C.; Oliphant, T. E. Array Programming with NumPy. *Nature* **2020**, *585* (7825), 357–362. https://doi.org/10.1038/s41586-020-2649-2.

(62) Virtanen, P.; Gommers, R.; Oliphant, T. E.; Haberland, M.; Reddy, T.; Cournapeau, D.; Burovski, E.; Peterson, P.; Weckesser, W.; Bright, J.; van der Walt, S. J.; Brett, M.; Wilson, J.; Millman, K. J.; Mayorov, N.; Nelson, A. R. J.; Jones, E.; Kern, R.; Larson, E.; Carey, C. J.; Polat, İ.; Feng, Y.; Moore, E. W.; VanderPlas, J.; Laxalde, D.; Perktold, J.; Cimrman, R.; Henriksen, I.; Quintero, E. A.; Harris, C. R.; Archibald, A. M.; Ribeiro, A. H.; Pedregosa, F.; van Mulbregt, P. SciPy 1.0: Fundamental Algorithms for Scientific Computing in Python. *Nat. Methods* **2020**, *17* (3), 261–272. https://doi.org/10.1038/s41592-019-0686-2.

(63) Pedregosa, F.; Varoquaux, G.; Gramfort, A.; Michel, V.; Thirion, B.; Grisel, O.; Blondel, M.; Prettenhofer, P.; Weiss, R.; Dubourg, V.; Vanderplas, J.; Passos, A.; Cournapeau, D. Scikit-Learn: Machine Learning in Python. *Mach. Learn. PYTHON* 6.

(64) Rycroft, C. H. VORO++: A Three-Dimensional Voronoi Cell Library in C++. *Chaos Interdiscip. J. Nonlinear Sci.* **2009**, *19* (4), 041111. https://doi.org/10.1063/1.3215722.

(65) Hunter, J. D. Matplotlib: A 2D Graphics Environment. *Comput. Sci. Eng.* **2007**, *9*, 90–95. https://doi.org/10.1109/MCSE.2007.55.

(66) Humphrey, W.; Dalke, A.; Schulten, K. VMD: Visual Molecular Dynamics. *J. Mol. Graph.* **1996**, *14* (1), 33–38, 27–28. https://doi.org/10.1016/0263-7855(96)00018-5.

(67) Sousa, F. M.; Lima, L. M. P.; Arnarez, C.; Pereira, M. M.; Melo, M. N. Coarse-Grained Parameterization of Nucleotide Cofactors and Metabolites: Protonation Constants, Partition Coefficients, and Model Topologies. *J. Chem. Inf. Model.* **2021**, *61* (1), 335–346. https://doi.org/10.1021/acs.jcim.0c01077.

(68) Huang, J.; MacKerell Jr, A. D. CHARMM36 All-Atom Additive Protein Force Field: Validation Based on Comparison to NMR Data. *J. Comput. Chem.* **2013**, *34* (25), 2135–2145. https://doi.org/10.1002/jcc.23354.

(69) Huang, J.; Rauscher, S.; Nawrocki, G.; Ran, T.; Feig, M.; de Groot, B. L.; Grubmüller, H.; MacKerell, A. D. CHARMM36m: An Improved Force Field for Folded and Intrinsically Disordered Proteins. *Nat. Methods* **2017**, *14* (1), 71–73. https://doi.org/10.1038/nmeth.4067.

(70) Jo, S.; Kim, T.; Iyer, V. G.; Im, W. CHARMM-GUI: A Web-Based Graphical User Interface for CHARMM. *J. Comput. Chem.* **2008**, *29* (11), 1859–1865. https://doi.org/10.1002/jcc.20945.

(71) Lee, J.; Cheng, X.; Swails, J. M.; Yeom, M. S.; Eastman, P. K.; Lemkul, J. A.; Wei, S.; Buckner, J.; Jeong, J. C.; Qi, Y.; Jo, S.; Pande, V. S.; Case, D. A.; Brooks, C. L.; MacKerell, A. D.; Klauda, J. B.; Im, W. CHARMM-GUI Input Generator for NAMD, GROMACS, AMBER, OpenMM, and CHARMM/OpenMM Simulations Using the CHARMM36 Additive Force Field. *J. Chem. Theory Comput.* **2016**, *12* (1), 405–413. https://doi.org/10.1021/acs.jctc.5b00935.

(72) Jo, S.; Lim, J. B.; Klauda, J. B.; Im, W. CHARMM-GUI Membrane Builder for Mixed Bilayers and Its Application to Yeast Membranes. *Biophys. J.* **2009**, *97* (1), 50–58. https://doi.org/10.1016/j.bpj.2009.04.013.

(73) Jo, S.; Kim, T.; Im, W. Automated Builder and Database of Protein/Membrane Complexes for Molecular Dynamics Simulations. *PLOS ONE* **2007**, *2* (9), e880. https://doi.org/10.1371/journal.pone.0000880.

(74) *CHARMM-GUI Membrane Builder for Complex Biological Membrane Simulations with Glycolipids and Lipoglycans | Journal of Chemical Theory and Computation*. https://pubs.acs.org/doi/10.1021/acs.jctc.8b01066 (accessed 2022-07-08).

(75) Hess, B.; Bekker, H.; Berendsen, H. J. C.; Fraaije, J. G. E. M. LINCS: A Linear Constraint Solver for Molecular Simulations. *J. Comput. Chem.* **1997**, *18* (12), 1463–1472. https://doi.org/10.1002/(SICI)1096-987X(199709)18:12<1463::AID-JCC4>3.0.CO;2-H.

(76) Darden, T.; York, D.; Pedersen, L. Particle Mesh Ewald: An N·log(N) Method for Ewald Sums in Large Systems. *J. Chem. Phys.* **1993**, *98* (12), 10089–10092. https://doi.org/10.1063/1.464397.

(77) Evans, D. J.; Holian, B. L. The Nose–Hoover Thermostat. *J. Chem. Phys.* **1985**, *83* (8), 4069–4074. https://doi.org/10.1063/1.449071.

(78) Parrinello, M.; Rahman, A. Polymorphic Transitions in Single Crystals: A New Molecular Dynamics Method. *J. Appl. Phys.* **1981**, *52* (12), 7182–7190. https://doi.org/10.1063/1.328693.
(79) Wassenaar, T. A.; Ingólfsson, H. I.; Böckmann, R. A.; Tieleman, D. P.; Marrink, S. J. Computational Lipidomics with Insane: A Versatile Tool for Generating Custom Membranes for Molecular Simulations. *J. Chem. Theory Comput.* **2015**, *11* (5), 2144–2155. https://doi.org/10.1021/acs.jctc.5b00209.
(80) Bogren, H.; Larsson, K. An X-Ray-Diffraction Study of Crystalline Cholesterol in Some Pathological Deposits in Man. *Biochim. Biophys. Acta* **1963**, *75*, 65–69. https://doi.org/10.1016/0006-3002(63)90580-8.
(81) Shieh, H.-S.; Hoard, L. G.; Nordman, C. E. The Structure of Cholesterol. *Acta Crystallogr. B* **1981**, *37* (8), 1538–1543. https://doi.org/10.1107/S0567740881006523.
(82) Berman, H. M.; Westbrook, J.; Feng, Z.; Gilliland, G.; Bhat, T. N.; Weissig, H.; Shindyalov, I. N.; Bourne, P. E. The Protein Data Bank. *Nucleic Acids Res.* **2000**, *28* (1), 235–242. https://doi.org/10.1093/nar/28.1.235.
(83) Byrne, E. F. X.; Sircar, R.; Miller, P. S.; Hedger, G.; Luchetti, G.; Nachtergaele, S.; Tully, M. D.; Mydock-McGrane, L.; Covey, D. F.; Rambo, R. P.; Sansom, M. S. P.; Newstead, S.; Rohatgi, R.; Siebold, C. Structural Basis of Smoothened Regulation by Its Extracellular Domains. *Nature* **2016**, *535* (7613), 517–522. https://doi.org/10.1038/nature18934.
(84) Hedger, G.; Koldsø, H.; Chavent, M.; Siebold, C.; Rohatgi, R.; Sansom, M. S. P. Cholesterol Interaction Sites on the Transmembrane Domain of the Hedgehog Signal Transducer and Class F G Protein-Coupled Receptor Smoothened. *Structure* **2019**, *27* (3), 549-559.e2. https://doi.org/10.1016/j.str.2018.11.003.
(85) Choudhary, O. P.; Paz, A.; Adelman, J. L.; Colletier, J.-P.; Abramson, J.; Grabe, M. Structure-Guided Simulations Illuminate the Mechanism of ATP Transport through VDAC1. *Nat. Struct. Mol. Biol.* **2014**, *21* (7), 626–632. https://doi.org/10.1038/nsmb.2841.
(86) Dadsena, S.; Bockelmann, S.; Mina, J. G. M.; Hassan, D. G.; Korneev, S.; Razzera, G.; Jahn, H.; Niekamp, P.; Müller, D.; Schneider, M.; Tafesse, F. G.; Marrink, S. J.; Melo, M. N.; Holthuis, J. C. M. Ceramides Bind VDAC2 to Trigger Mitochondrial Apoptosis. *Nat. Commun.* **2019**, *10* (1), 1832. https://doi.org/10.1038/s41467-019-09654-4.
(87) Hanson, M. A.; Cherezov, V.; Griffith, M. T.; Roth, C. B.; Jaakola, V.-P.; Chien, E. Y. T.; Velasquez, J.; Kuhn, P.; Stevens, R. C. A Specific Cholesterol Binding Site Is Established by the 2.8 Å Structure of the Human B2-Adrenergic Receptor. *Structure* **2008**, *16* (6), 897–905. https://doi.org/10.1016/j.str.2008.05.001.
(88) Kroon, P. C.; Grünewald, F.; Barnoud, J.; van Tilburg, M.; Souza, P. C. T.; Wassenaar, T. A.; Marrink, S.-J. Martinize2 and Vermouth: Unified Framework for Topology Generation. **2022**. https://doi.org/10.48550/ARXIV.2212.01191.
(89) Herzog, F. A.; Braun, L.; Schoen, I.; Vogel, V. Improved Side Chain Dynamics in MARTINI Simulations of Protein–Lipid Interfaces. *J. Chem. Theory Comput.* **2016**, *12* (5), 2446–2458. https://doi.org/10.1021/acs.jctc.6b00122.
(90) de Jong, D. H.; Baoukina, S.; Ingólfsson, H. I.; Marrink, S. J. Martini Straight: Boosting Performance Using a Shorter Cutoff and GPUs. *Comput. Phys. Commun.* **2016**, *199*, 1–7. https://doi.org/10.1016/j.cpc.2015.09.014.
(91) Bussi, G.; Donadio, D.; Parrinello, M. Canonical Sampling through Velocity Rescaling. *J. Chem. Phys.* **2007**, *126* (1), 014101. https://doi.org/10.1063/1.2408420.
(92) Fábián, B.; Thallmair, S.; Hummer, G. Small Ionic Radii Limit Time Step in Martini 3 Molecular Dynamics Simulations. *J. Chem. Phys.* **2022**, *157* (3), 034101. https://doi.org/10.1063/5.0095523.
(93) Nemkevich, A.; Bürgi, H.-B.; Spackman, M. A.; Corry, B. Molecular Dynamics Simulations of Structure and Dynamics of Organic Molecular Crystals. *Phys. Chem. Chem. Phys.* **2010**, *12* (45), 14916–14929. https://doi.org/10.1039/C0CP01409E.
(94) Eastman, P.; Swails, J.; Chodera, J. D.; McGibbon, R. T.; Zhao, Y.; Beauchamp, K. A.; Wang, L.-P.; Simmonett, A. C.; Harrigan, M. P.; Stern, C. D.; Wiewiora, R. P.; Brooks, B. R.; Pande, V. S. OpenMM 7: Rapid Development of High Performance Algorithms for Molecular Dynamics. *PLOS Comput. Biol.* **2017**, *13* (7), e1005659. https://doi.org/10.1371/journal.pcbi.1005659.
(95) MacCallum, J. L.; Hu, S.; Lenz, S.; Souza, P. C. T.; Corradi, V.; Tieleman, D. P. An

Implementation of the Martini Coarse-Grained Force Field in OpenMM. *Biophys. J.* **2023**. https://doi.org/10.1016/j.bpj.2023.04.007.
(96) Melo, M. N.; Ingólfsson, H. I.; Marrink, S. J. Parameters for Martini Sterols and Hopanoids Based on a Virtual-Site Description. *J. Chem. Phys.* **2015**, *143* (24), 243152. https://doi.org/10.1063/1.4937783.
(97) Bulacu, M.; Goga, N.; Zhao, W.; Rossi, G.; Monticelli, L.; Periole, X.; Tieleman, D. P.; Marrink, S. J. Improved Angle Potentials for Coarse-Grained Molecular Dynamics Simulations. *J. Chem. Theory Comput.* **2013**, *9* (8), 3282–3292. https://doi.org/10.1021/ct400219n.
(98) Eastman, P.; Pande, V. S. Constant Constraint Matrix Approximation: A Robust, Parallelizable Constraint Method for Molecular Simulations. *J. Chem. Theory Comput.* **2010**, *6* (2), 434–437. https://doi.org/10.1021/ct900463w.
(99) Sapay, N.; Tieleman, D. P. Combination of the CHARMM27 Force Field with United-Atom Lipid Force Fields. *J. Comput. Chem.* **2011**, *32* (7), 1400–1410. https://doi.org/10.1002/jcc.21726.
(100) Bjelkmar, P.; Larsson, P.; Cuendet, M. A.; Hess, B.; Lindahl, E. Implementation of the CHARMM Force Field in GROMACS: Analysis of Protein Stability Effects from Correction Maps, Virtual Interaction Sites, and Water Models. *J. Chem. Theory Comput.* **2010**, *6* (2), 459–466. https://doi.org/10.1021/ct900549r.
(101) Lim, J. B.; Rogaski, B.; Klauda, J. B. Update of the Cholesterol Force Field Parameters in CHARMM. *J. Phys. Chem. B* **2012**, *116* (1), 203–210. https://doi.org/10.1021/jp207925m.
(102) Marquardt, D.; Kučerka, N.; Wassall, S. R.; Harroun, T. A.; Katsaras, J. Cholesterol's Location in Lipid Bilayers. *Chem. Phys. Lipids* **2016**, *199*, 17–25. https://doi.org/10.1016/j.chemphyslip.2016.04.001.
(103) Harroun, T. A.; Katsaras, J.; Wassall, S. R. *Cholesterol Is Found To Reside in the Center of a Polyunsaturated Lipid Membrane*. ACS Publications. https://doi.org/10.1021/bi800123b.
(104) Marquardt, D.; Heberle, F. A.; Greathouse, D. V.; Koeppe, R. E.; Standaert, R. F.; Oosten, B. J. V.; Harroun, T. A.; Kinnun, J. J.; Williams, J. A.; Wassall, S. R.; Katsaras, J. Lipid Bilayer Thickness Determines Cholesterol's Location in Model Membranes. *Soft Matter* **2016**, *12* (47), 9417–9428. https://doi.org/10.1039/C6SM01777K.
(105) Bennett, W. F. D.; MacCallum, J. L.; Hinner, M. J.; Marrink, S. J.; Tieleman, D. P. Molecular View of Cholesterol Flip-Flop and Chemical Potential in Different Membrane Environments. *J. Am. Chem. Soc.* **2009**, *131* (35), 12714–12720. https://doi.org/10.1021/ja903529f.
(106) Martinez-Seara, H.; Róg, T.; Karttunen, M.; Vattulainen, I.; Reigada, R. Cholesterol Induces Specific Spatial and Orientational Order in Cholesterol/Phospholipid Membranes. *PLOS ONE* **2010**, *5* (6), e11162. https://doi.org/10.1371/journal.pone.0011162.
(107) Drolle, E.; Kučerka, N.; Hoopes, M. I.; Choi, Y.; Katsaras, J.; Karttunen, M.; Leonenko, Z. Effect of Melatonin and Cholesterol on the Structure of DOPC and DPPC Membranes. *Biochim. Biophys. Acta BBA - Biomembr.* **2013**, *1828* (9), 2247–2254. https://doi.org/10.1016/j.bbamem.2013.05.015.
(108) Martinez-Seara, H.; Róg, T.; Pasenkiewicz-Gierula, M.; Vattulainen, I.; Karttunen, M.; Reigada, R. Interplay of Unsaturated Phospholipids and Cholesterol in Membranes: Effect of the Double-Bond Position. *Biophys. J.* **2008**, *95* (7), 3295–3305. https://doi.org/10.1529/biophysj.108.138123.
(109) Javanainen, M.; Heftberger, P.; Madsen, J. J.; Miettinen, M. S.; Pabst, G.; Ollila, O. H. S. Quantitative Comparison against Experiments Reveals Imperfections in Force Fields' Descriptions of POPC–Cholesterol Interactions. *J. Chem. Theory Comput.* **2023**. https://doi.org/10.1021/acs.jctc.3c00648.
(110) MacDermaid, C. M.; Kashyap, H. K.; DeVane, R. H.; Shinoda, W.; Klauda, J. B.; Klein, M. L.; Fiorin, G. Molecular Dynamics Simulations of Cholesterol-Rich Membranes Using a Coarse-Grained Force Field for Cyclic Alkanes. *J. Chem. Phys.* **2015**, *143* (24), 243144. https://doi.org/10.1063/1.4937153.
(111) Hung, W.-C.; Lee, M.-T.; Chen, F.-Y.; Huang, H. W. The Condensing Effect of Cholesterol in Lipid Bilayers. *Biophys. J.* **2007**, *92* (11), 3960–3967. https://doi.org/10.1529/biophysj.106.099234.
(112) Poger, D.; Caron, B.; Mark, A. E. Validating Lipid Force Fields against Experimental Data: Progress, Challenges and Perspectives. *Biochim. Biophys. Acta BBA - Biomembr.* **2016**,

1858 (7), 1556–1565. https://doi.org/10.1016/j.bbamem.2016.01.029.
(113) Sodt, A. J.; Sandar, M. L.; Gawrisch, K.; Pastor, R. W.; Lyman, E. The Molecular Structure of the Liquid-Ordered Phase of Lipid Bilayers. *J. Am. Chem. Soc.* **2014**, *136* (2), 725–732. https://doi.org/10.1021/ja4105667.
(114) Armstrong, C. L.; Marquardt, D.; Dies, H.; Kučerka, N.; Yamani, Z.; Harroun, T. A.; Katsaras, J.; Shi, A.-C.; Rheinstädter, M. C. The Observation of Highly Ordered Domains in Membranes with Cholesterol. *PLOS ONE* **2013**, *8* (6), e66162. https://doi.org/10.1371/journal.pone.0066162.
(115) Schachter, I.; Paananen, R. O.; Fábián, B.; Jurkiewicz, P.; Javanainen, M. The Two Faces of the Liquid Ordered Phase. *J. Phys. Chem. Lett.* **2022**, *13* (5), 1307–1313. https://doi.org/10.1021/acs.jpclett.1c03712.
(116) *Handbook of Lipid Bilayers*. Routledge & CRC Press. https://www.routledge.com/Handbook-of-Lipid-Bilayers/Marsh/p/book/9781420088328 (accessed 2022-08-11).
(117) Korlach, J.; Baumgart, T.; Webb, W. W.; Feigenson, G. W. Detection of Motional Heterogeneities in Lipid Bilayer Membranes by Dual Probe Fluorescence Correlation Spectroscopy. *Biochim. Biophys. Acta BBA - Biomembr.* **2005**, *1668* (2), 158–163. https://doi.org/10.1016/j.bbamem.2004.11.016.
(118) Feigenson, G. W.; Buboltz, J. T. Ternary Phase Diagram of Dipalmitoyl-PC/Dilauroyl-PC/Cholesterol: Nanoscopic Domain Formation Driven by Cholesterol. *Biophys. J.* **2001**, *80* (6), 2775–2788. https://doi.org/10.1016/S0006-3495(01)76245-5.
(119) Huang, T. H.; Lee, C. W. B.; Das Gupta, S. K.; Blume, A.; Griffin, R. G. A Carbon-13 and Deuterium Nuclear Magnetic Resonance Study of Phosphatidylcholine/Cholesterol Interactions: Characterization of Liquid-Gel Phases. *Biochemistry* **1993**, *32* (48), 13277–13287. https://doi.org/10.1021/bi00211a041.
(120) McMullen, T. P. W.; McElhaney, R. N. New Aspects of the Interaction of Cholesterol with Dipalmitoylphosphatidylcholine Bilayers as Revealed by High-Sensitivity Differential Scanning Calorimetry. *Biochim. Biophys. Acta BBA - Biomembr.* **1995**, *1234* (1), 90–98. https://doi.org/10.1016/0005-2736(94)00266-R.
(121) Sankaram, M. B.; Thompson, T. E. Cholesterol-Induced Fluid-Phase Immiscibility in Membranes. *Proc. Natl. Acad. Sci.* **1991**, *88* (19), 8686–8690. https://doi.org/10.1073/pnas.88.19.8686.
(122) Chiang, Y.-W.; Costa-Filho, A. J.; Freed, J. H. Dynamic Molecular Structure and Phase Diagram of DPPC−Cholesterol Binary Mixtures: A 2D-ELDOR Study. *J. Phys. Chem. B* **2007**, *111* (38), 11260–11270. https://doi.org/10.1021/jp0732110.
(123) Veatch, S. L.; Soubias, O.; Keller, S. L.; Gawrisch, K. Critical Fluctuations in Domain-Forming Lipid Mixtures. *Proc. Natl. Acad. Sci. U. S. A.* **2007**, *104* (45), 17650–17655. https://doi.org/10.1073/pnas.0703513104.
(124) Empereur-mot, C.; Pedersen, K. B.; Capelli, R.; Crippa, M.; Caruso, C.; Perrone, M.; Souza, P. C. T.; Marrink, S. J.; Pavan, G. M. On the Automatic Optimization of Lipid Models in the Martini Force Field Using SwarmCG. ChemRxiv April 6, 2023. https://doi.org/10.26434/chemrxiv-2023-q5rvm-v2.
(125) Gu, R.-X.; Baoukina, S.; Tieleman, D. P. Phase Separation in Atomistic Simulations of Model Membranes. *J. Am. Chem. Soc.* **2020**. https://doi.org/10.1021/jacs.9b11057.
(126) Tzortzini, E.; Corey, R. A.; Kolocouris, A. Comparative Study of Receptor-, Receptor State-, and Membrane-Dependent Cholesterol Binding Sites in A2A and A1 Adenosine Receptors Using Coarse-Grained Molecular Dynamics Simulations. *J. Chem. Inf. Model.* **2023**, *63* (3), 928–949. https://doi.org/10.1021/acs.jcim.2c01181.
(127) Johnson, M. Molecular Mechanisms of B2-Adrenergic Receptor Function, Response, and Regulation. *J. Allergy Clin. Immunol.* **2006**, *117* (1), 18–24. https://doi.org/10.1016/j.jaci.2005.11.012.
(128) Bylund, D. B. Beta-2 Adrenoceptor*. In *xPharm: The Comprehensive Pharmacology Reference*; Enna, S. J., Bylund, D. B., Eds.; Elsevier: New York, 2007; pp 1–12. https://doi.org/10.1016/B978-008055232-3.60201-6.
(129) Reinhart, C.; Weiss, H. M.; Reiländer, H. 9 - Purification of an Affinity-Epitope Tagged G-Protein Coupled Receptor. In *Membrane Protein Purification and Crystallization (Second Edition)*; Hunte, C., Von jagow, G., Schägger, H., Eds.; Academic Press: San Diego, 2003;

pp 167–178. https://doi.org/10.1016/B978-012361776-7/50010-3.
(130) Cherezov, V.; Rosenbaum, D. M.; Hanson, M. A.; Rasmussen, S. G. F.; Thian, F. S.; Kobilka, T. S.; Choi, H.-J.; Kuhn, P.; Weis, W. I.; Kobilka, B. K.; Stevens, R. C. High-Resolution Crystal Structure of an Engineered Human Beta2-Adrenergic G Protein-Coupled Receptor. *Science* **2007**, *318* (5854), 1258–1265. https://doi.org/10.1126/science.1150577.
(131) Ma, P.; Weichert, D.; Aleksandrov, L. A.; Jensen, T. J.; Riordan, J. R.; Liu, X.; Kobilka, B. K.; Caffrey, M. The Cubicon Method for Concentrating Membrane Proteins in the Cubic Mesophase. *Nat. Protoc.* **2017**, *12* (9), 1745–1762. https://doi.org/10.1038/nprot.2017.057.
(132) Manna, M.; Niemelä, M.; Tynkkynen, J.; Javanainen, M.; Kulig, W.; Müller, D. J.; Rog, T.; Vattulainen, I. Mechanism of Allosteric Regulation of B2-Adrenergic Receptor by Cholesterol. *eLife 5*, e18432. https://doi.org/10.7554/eLife.18432.
(133) Cang, X.; Du, Y.; Mao, Y.; Wang, Y.; Yang, H.; Jiang, H. Mapping the Functional Binding Sites of Cholesterol in B2-Adrenergic Receptor by Long-Time Molecular Dynamics Simulations. *J. Phys. Chem. B* **2013**, *117* (4), 1085–1094. https://doi.org/10.1021/jp3118192.
(134) Lee, J. Y.; Lyman, E. Predictions for Cholesterol Interaction Sites on the A2A Adenosine Receptor. *J. Am. Chem. Soc.* **2012**, *134* (40), 16512–16515. https://doi.org/10.1021/ja307532d.
(135) Weiser, B. P.; Salari, R.; Eckenhoff, R. G.; Brannigan, G. Computational Investigation of Cholesterol Binding Sites on Mitochondrial VDAC. *J. Phys. Chem. B* **2014**, *118* (33), 9852–9860. https://doi.org/10.1021/jp504516a.
(136) Budelier, M. M.; Cheng, W. W. L.; Bergdoll, L.; Chen, Z.-W.; Janetka, J. W.; Abramson, J.; Krishnan, K.; Mydock-McGrane, L.; Covey, D. F.; Whitelegge, J. P.; Evers, A. S. Photoaffinity Labeling with Cholesterol Analogues Precisely Maps a Cholesterol-Binding Site in Voltage-Dependent Anion Channel-1. *J. Biol. Chem.* **2017**, *292* (22), 9294–9304. https://doi.org/10.1074/jbc.M116.773069.
(137) Cheng, W. W. L.; Budelier, M. M.; Sugasawa, Y.; Bergdoll, L.; Queralt-Martín, M.; Rosencrans, W.; Rostovtseva, T. K.; Chen, Z.-W.; Abramson, J.; Krishnan, K.; Covey, D. F.; Whitelegge, J. P.; Evers, A. S. Multiple Neurosteroid and Cholesterol Binding Sites in Voltage-Dependent Anion Channel-1 Determined by Photo-Affinity Labeling. *Biochim. Biophys. Acta Mol. Cell Biol. Lipids* **2019**, *1864* (10), 1269–1279. https://doi.org/10.1016/j.bbalip.2019.06.004.
(138) Cang, X.; Yang, L.; Yang, J.; Luo, C.; Zheng, M.; Yu, K.; Yang, H.; Jiang, H. Cholesterol-β1AR Interaction versus Cholesterol-β2AR Interaction. *Proteins Struct. Funct. Bioinforma.* **2014**, *82* (5), 760–770. https://doi.org/10.1002/prot.24456.
(139) Valério, M.; Mendonça, D. A.; Morais, J.; Buga, C. C.; Cruz, C. H.; Castanho, M. A. R. B.; Melo, M. N.; Soares, C. M.; Veiga, A. S.; Lousa, D. Parainfluenza Fusion Peptide Promotes Membrane Fusion by Assembling into Oligomeric Porelike Structures. *ACS Chem. Biol.* **2022**, *17* (7), 1831–1843. https://doi.org/10.1021/acschembio.2c00208.
(140) Spinti, J. K.; Neiva Nunes, F.; Melo, M. N. Room for Improvement in the Initial Martini 3 Parameterization of Peptide Interactions. *Chem. Phys. Lett.* **2023**, *819*, 140436. https://doi.org/10.1016/j.cplett.2023.140436.
(141) Cabezudo, A. C.; Athanasiou, C.; Tsengenes, A.; Wade, R. C. Scaling Protein-Water Interactions in the Martini 3 Coarse-Grained Force Field to Simulate Transmembrane Helix Dimers in Different Lipid Environments. bioRxiv February 16, 2023, p 2022.09.09.506752. https://doi.org/10.1101/2022.09.09.506752.

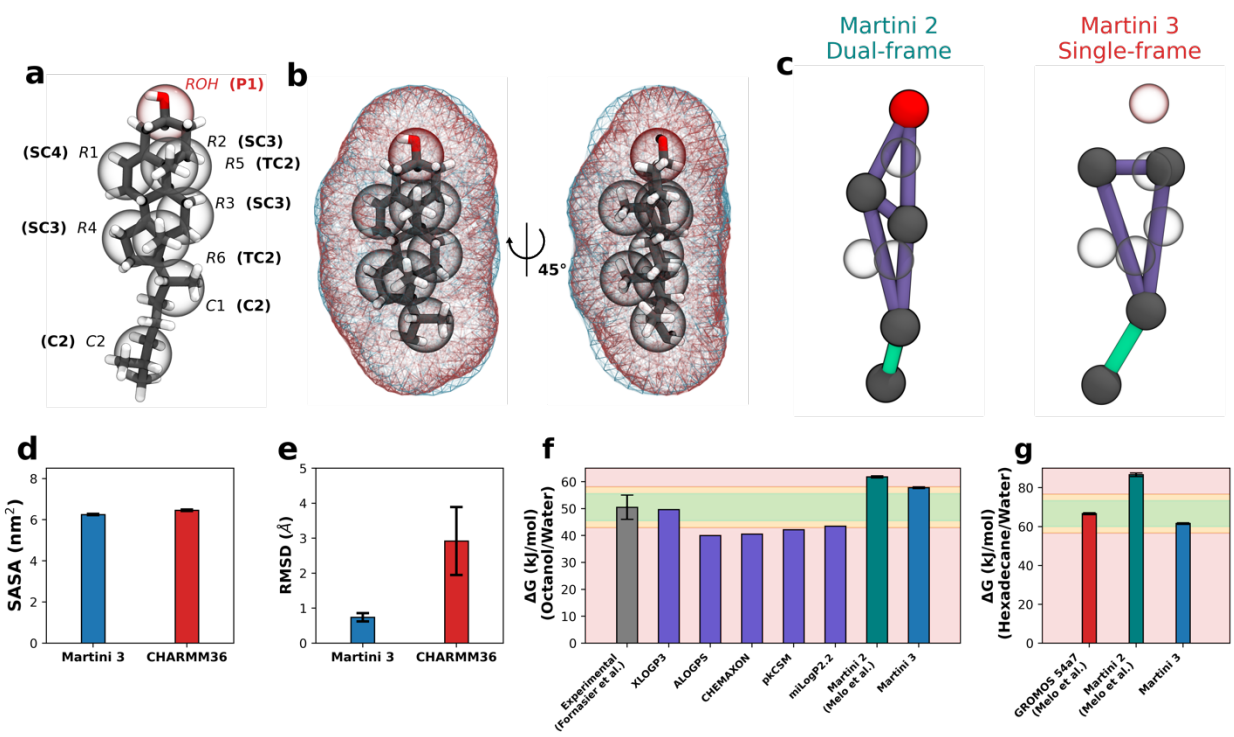

Figure 1. (a) Chemical structure and coarse-grained mapping of the cholesterol model parameterized in this work. Assigned Martini 3 bead names (italic) and types (bold) are indicated for each bead as overlaid gray text. (b) Connolly surfaces for the Martini 3 cholesterol model developed in this study (blue wireframe) as well as the atomistic reference (red wireframe). (c) Schematic representations of the dual-frame and single-frame virtual site models used by the Martini 2 and the Martini 3 cholesterol models, respectively. Purple and green bonds indicate linear constraints and harmonic bonds, respectively. Virtual sites beads are depicted by translucent spheres, while those defined by traditional bonded terms are shown full. Note the two triangular constraint frames in the Martini 2 model compared to the single triangular frame in the Martini 3 model. (d) SASA for the Martini 3 cholesterol model developed in this study (red) as well as the atomistic reference (blue). (e) RMSD compared to respective reference structures in MD trajectories of the Martini 3 and CG-mapped CHARMM36 cholesterol models. Error bars represent the standard deviation. (f) Octanol/water and (g) hexadecane/water partition free energy values for the Martini 2 and 3 cholesterol models as well as for theoretical and experimental references when available.

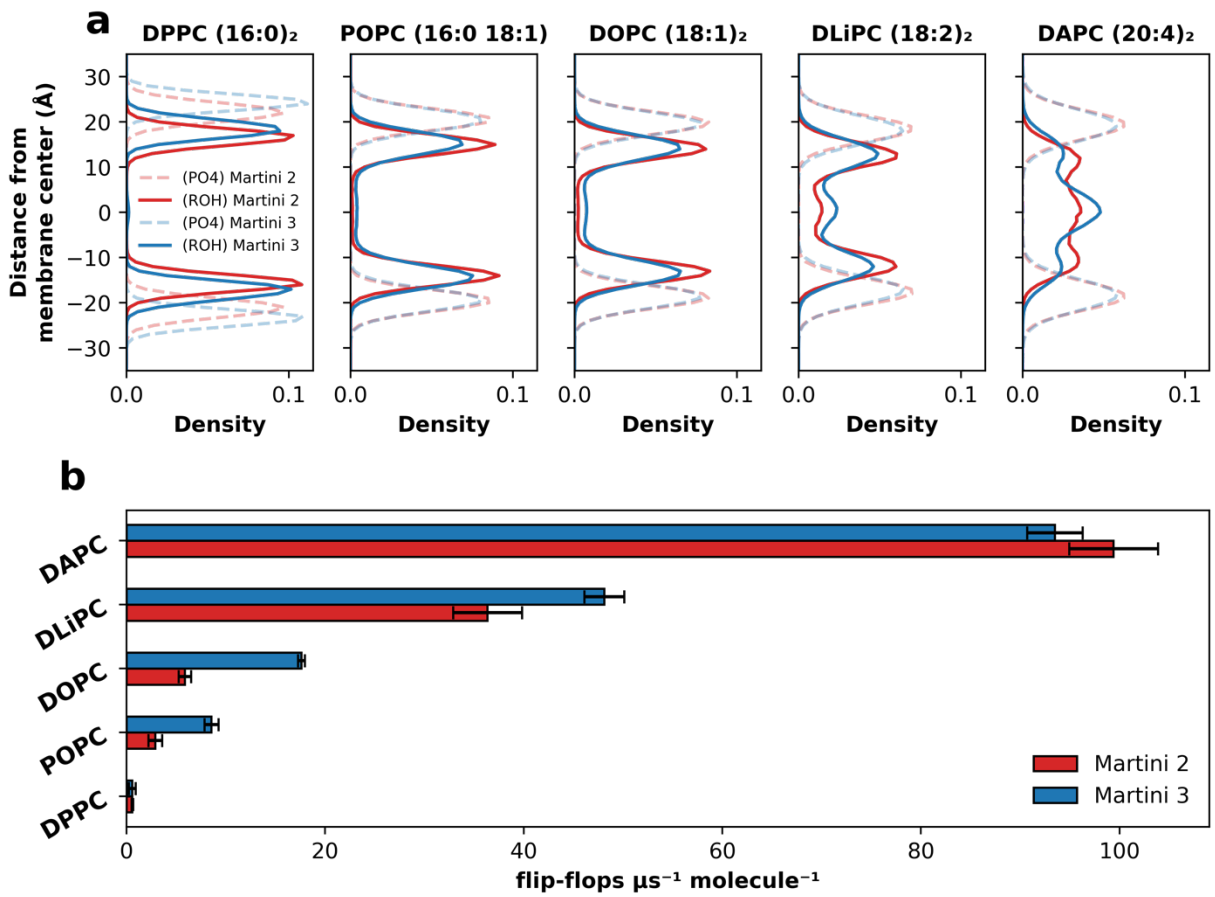

Figure 2. Cholesterol insertion in lipid bilayers. (a) Cholesterol membrane density profiles for the hydroxyl group (*ROH*, solid line) and neighboring lipid phosphodiester groups (*PO4*, dashed line) in several lipid bilayers of decreasing saturation. Profiles were determined for the Martini 2 and 3 CG models (red and blue, respectively). (b) Flip-flop rates for Martini 2 and 3 cholesterol models in several lipid bilayers of decreasing saturation (red and blue, respectively). Error bars represent the 95 % confidence interval of the mean estimated by bootstrapping.

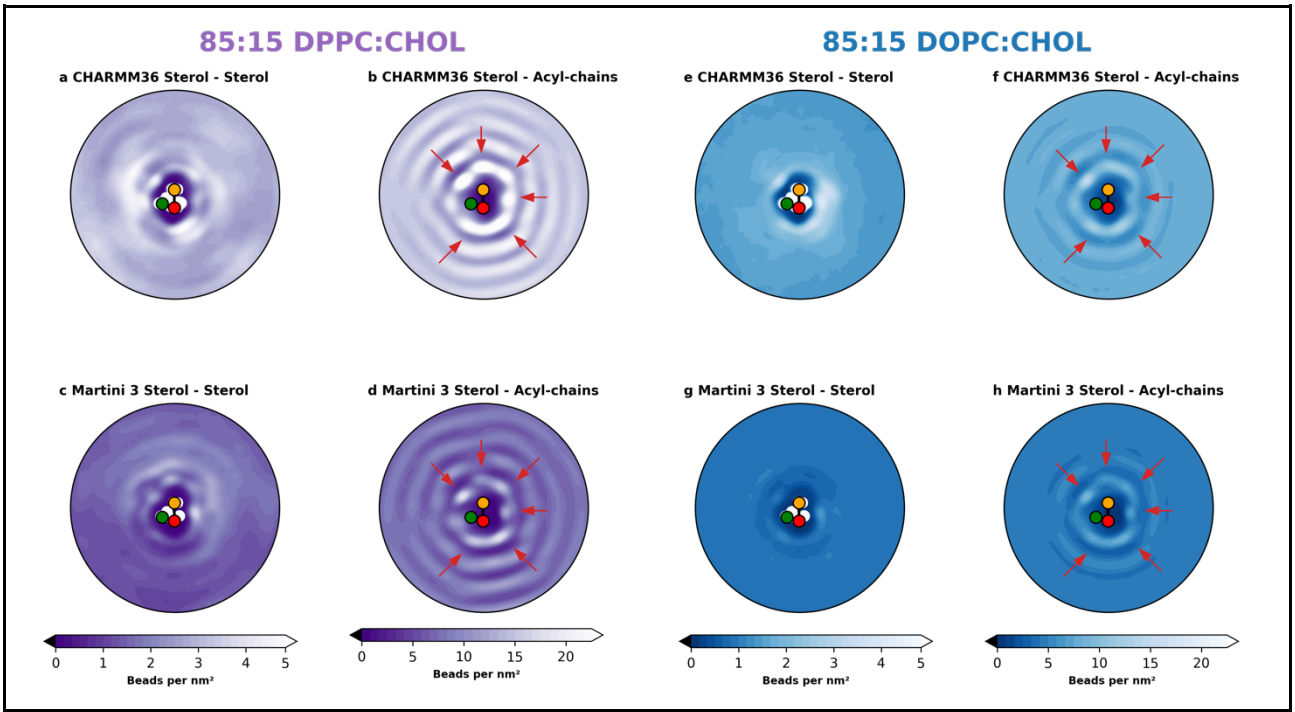

Figure 3. Spatial distribution of cholesterol neighbors in the bilayer plane. (b/d) and (f/h) represent DPPC/DOPC acyl bead distributions, respectively, and (a/c) and (e/g) represent cholesterol ring bead distributions, respectively. The bottom row (c,d,g,h) was obtained with the Martini 3 cholesterol model developed here, and the upper row (a,b,e,f) with the CHARMM atomistic reference. Orange, red and green markers represent the position of the *R1*, *R2* and *R5* beads, respectively. The first neighbor shell is located around 0.5 nm from the center of the reference cholesterol. Red arrows highlight the preferred PC interaction hotspots.

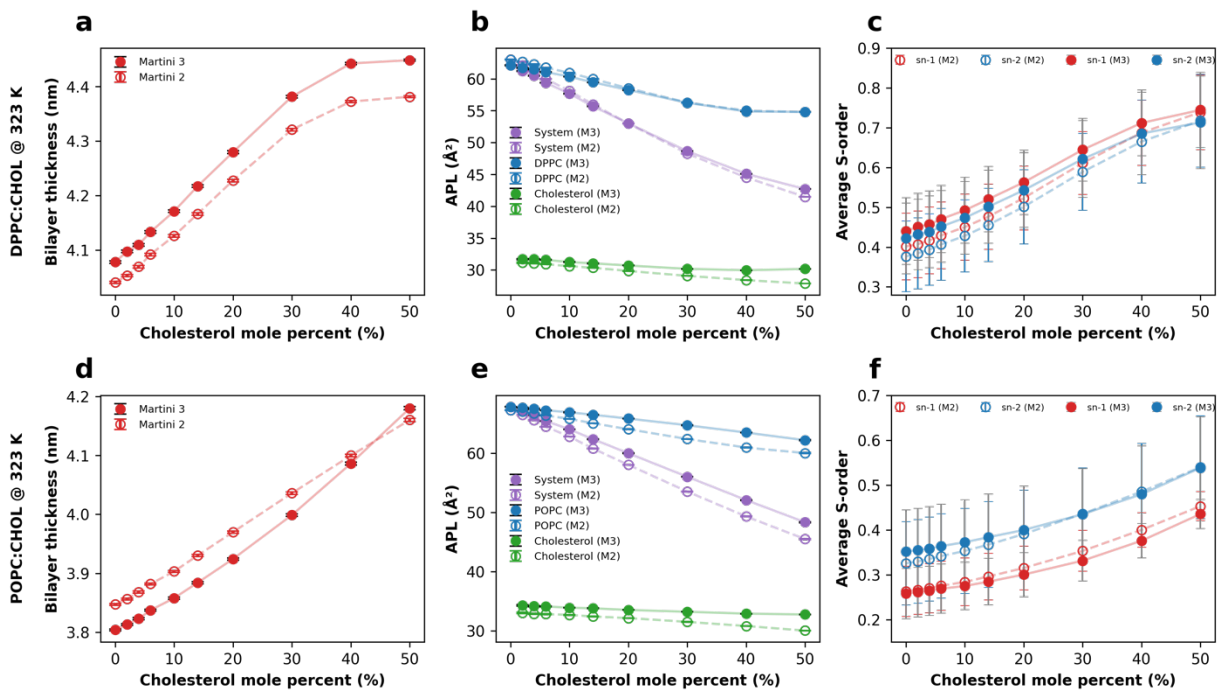

Figure 4. Impact of cholesterol on DPPC and POPC bilayers. Effect of increasing concentrations of cholesterol on (a,d) bilayer thickness, (b,e) APL and (c,f) average acyl chain order of DPPC (top row, a,b and c) and POPC (bottom row, d,e and f) membrane bilayers at 323 K. Error bars represent the 95 % confidence interval of the mean estimated by bootstrapping.

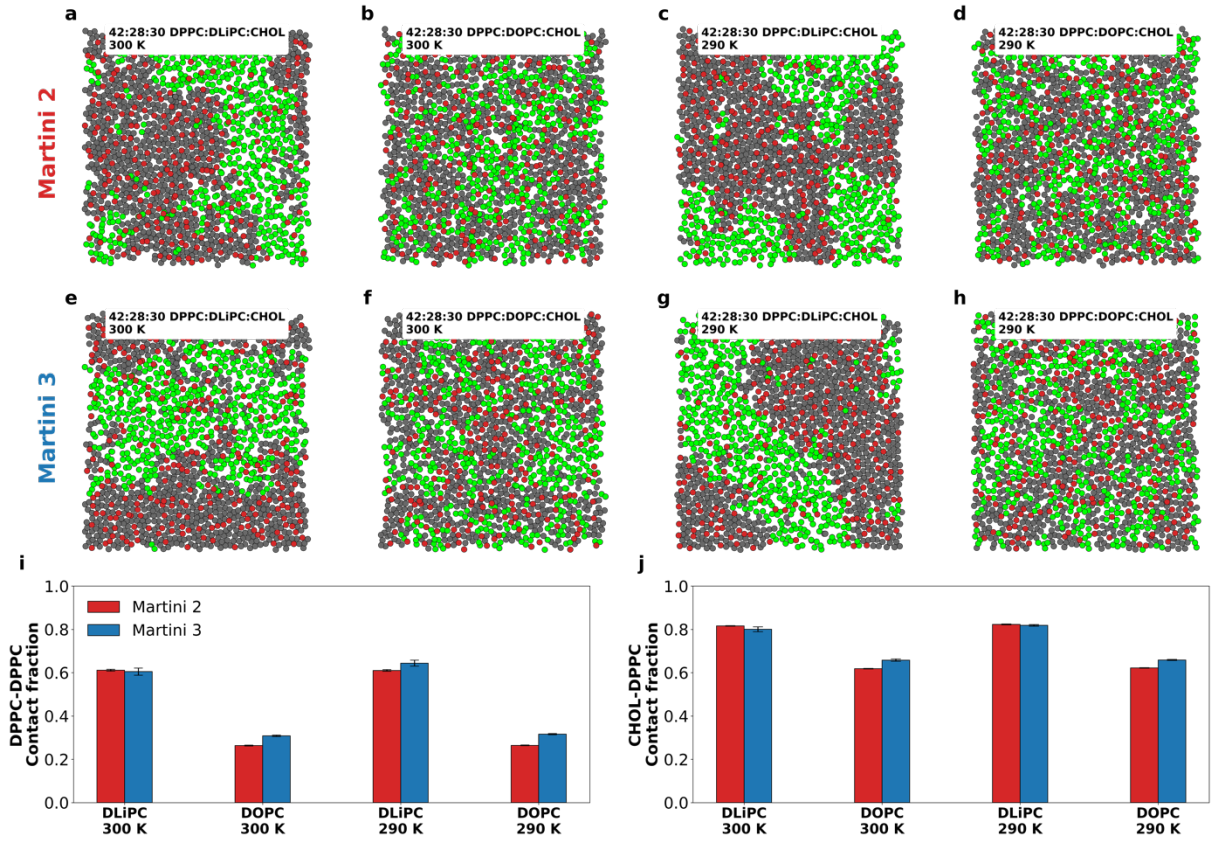

Figure 5. Impact of cholesterol on phase separation of ternary lipid membrane systems. Top views of 42:28:30 DPPC:DLiPC:Chol (a,c,e,g) and DPPC:DOPC:Chol (b,d,f,h) membranes, at 300 and 290 K (a,b,e,f and c,d,g,h, respectively), comparing the Lo phase behavior of the Martini 2 (a,b,c,d) and Martini 3 (e,f,g,h) cholesterol models. Spheres represent either the first lipid tail beads (DPPC in grey and unsaturated lipid in green) or the cholesterol *ROH* bead (red). (i) DPPC-DPPC and (j) CHOL-DPPC contact fractions for the Martini 2 and 3 models (red and blue, respectively). Higher contact fractions signify more segregated lipids, while lower contact fractions represent more mixed lipids. Error bars represent the 95 % confidence interval of the mean estimated by bootstrapping.

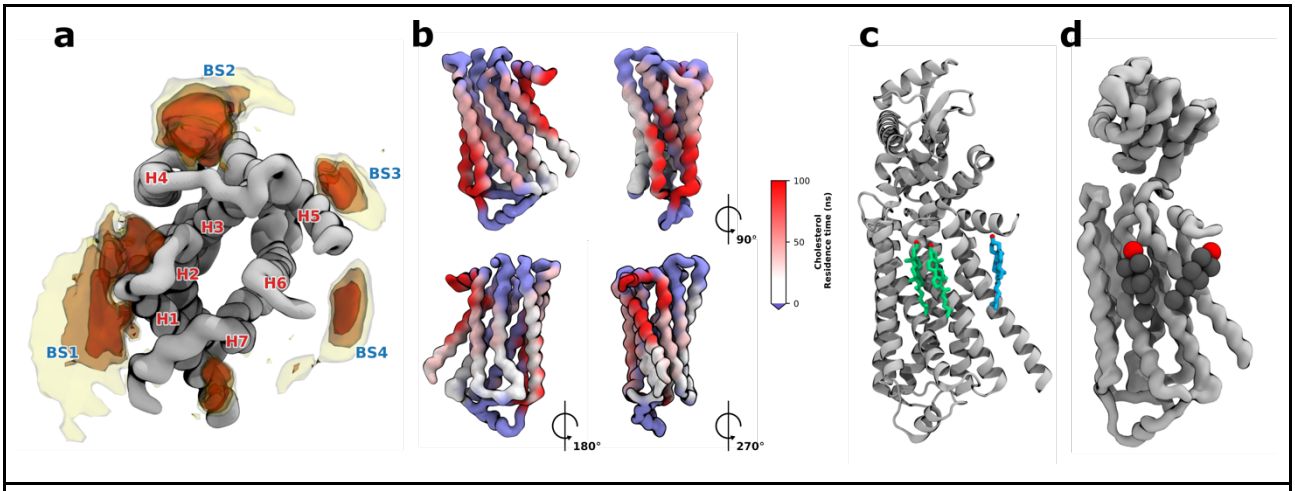

Figure 6. Cholesterol recognition and binding by β_2AR. (a) Occupancy map of Martini 3 cholesterol interactions with β_2AR. β_2AR helices are labeled in red and detected binding sites in blue. (b) β_2AR contact surface coloured by cholesterol residence time. (c) Cholesterol molecules bound to β_2AR as determined by X-ray diffraction (green cholesterol molecules detected in PDB:3D4S[87]; blue cholesterol molecules detected in PDB:2RH1[130]). (d) Snapshot of Martini 3 cholesterol bound to β_2AR.

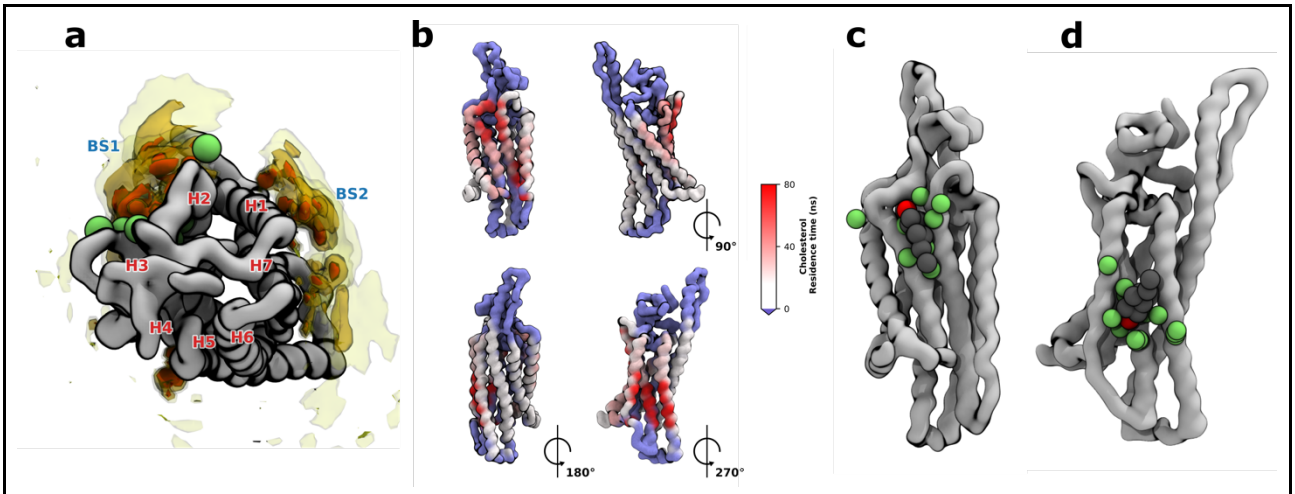

Figure 7. Cholesterol recognition and binding by SMO. (a) Occupancy map of Martini 3 cholesterol interactions with SMO. Green spheres represent side chains of interaction site described by Hedger *et al.*[84]. (b) SMO contact surface coloured by cholesterol residence time. (c) Snapshot of Martini 3 cholesterol bound to SMO in the binding site (green spheres) described by Hedger et al.[84]. (d) Snapshot of alternative cholesterol binding site in SMO detected with our Martini 3 model. Green spheres show side chains of this interaction site.

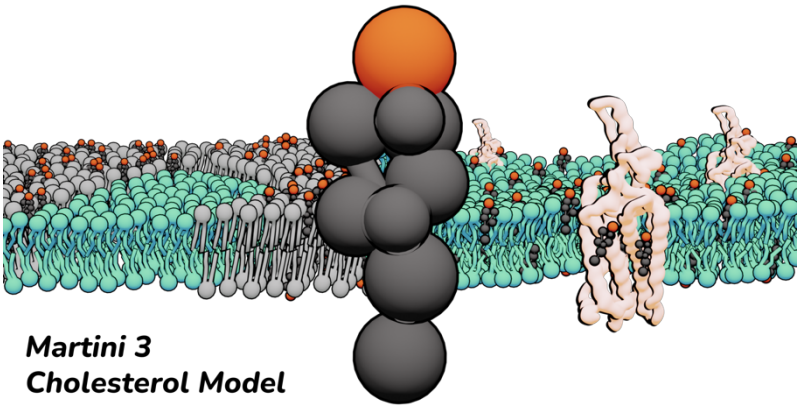

Table of contents / Abstract graphics